Medical Image Analysis 58 (2019) 101540

Contents lists available at ScienceDirect

Medical Image Analysis

journal homepage: www.elsevier.com/locate/media

Surface-constrained volumetric registration for the early developing brain

Sahar Ahmad[a], Zhengwang Wu[a], Gang Li[a], Li Wang[a], Weili Lin[a], Pew-Thian Yap[a,*], Dinggang Shen[a,b,*]

[a] Department of Radiology and Biomedical Research Imaging Center (BRIC), University of North Carolina, Chapel Hill, United States
[b] Department of Brain and Cognitive Engineering, Korea University, Seoul 02841, Republic of Korea

ARTICLE INFO

Article history:
Received 2 November 2018
Revised 26 July 2019
Accepted 29 July 2019
Available online 1 August 2019

Keywords:
Infant magnetic resonance imaging
Joint cortical surface and volumetric registration

ABSTRACT

The T1-weighted and T2-weighted MRI contrasts of the infant brain evolve drastically during the first year of life. This poses significant challenges to inter- and intra-subject registration, which is key to subsequent statistical analyses. Existing registration methods that do not consider temporal contrast changes are ineffective for infant brain MRI data. To address this problem, we present in this paper a method for deformable registration of infant brain MRI. The key advantage of our method is threefold: (i) To deal with appearance changes, registration is performed based on segmented tissue maps instead of image intensity. Segmentation is performed by using an infant-centric algorithm previously developed by our group. (ii) Registration is carried out with respect to both cortical surfaces and volumetric tissue maps, thus allowing precise alignment of both cortical and subcortical structures. (iii) A dynamic elasticity model is utilized to allow large non-linear deformation. Experimental results in comparison with well-established registration methods indicate that our method yields superior accuracy in both cortical and subcortical alignment.

1. Introduction

The infant brain grows and develops at a rapid pace during the first two years of life, resulting in drastic structural changes (Gilmore et al., 2018; Li et al., 2018, 2015a; Lyall et al., 2015; Meng et al., 2014; Nie et al., 2014, 2012; Geng et al., 2017). For instance, the overall brain volume doubles to about 65% of the adult brain volume in the first year of life (Knickmeyer et al., 2008). During this time span, gray matter (GM) grows more rapidly (108–149%) than white matter (WM) (∼11%) (Matsuzawa et al., 2001). Cortical thickness and surface area increase immensely from birth to one year of age. Understanding the longitudinal trajectory of early brain development is of critical importance for neuroscience and neuropsychology (Hazlett et al., 2017; Paterson et al., 2006).

To this end, a pivotal step for quantifying morphological changes is establishing anatomical correspondence using deformable registration (Shi et al., 2013; Li et al., 2014b; Nie et al., 2013; Xue et al., 2006a). However, deformable registration of infant brain data is challenging owing to rapid brain structural changes in relation to development, with cortical and subcortical structures exhibiting different growth trajectories (Choe et al., 2013). Brain tissues exhibit dynamic appearance changes over the first year of life (Fig. 1). More specifically, WM appears dark in the neonatal T1-weighted image as most of the WM is not yet myelinated, resulting in a low GM-WM contrast. As myelination progresses with development, WM gains a brighter appearance (Xue et al., 2007).

Existing deformable registration methods (Tang et al., 2018; Yang et al., 2017; Chen et al., 2017; Wu et al., 2016; Kim et al., 2015; Wang et al., 2015b; Avants et al., 2008; Wu et al., 2006; Xue et al., 2006b) are designed for adult brain images and have limited applicability to infant brain images. The key limiting factor of these methods is their inability to deal with dramatic appearance changes. Only a few registration methods are developed specifically for infant brain images. In (Wu et al., 2015), growth trajectories learned from a longitudinal image training set are used to guide registration. In (Wei et al., 2017), auto-context random forest regression is employed to learn structural shape and appearance changes from longitudinal infant brain data.

* Corresponding authors.
E-mail addresses: ptyap@med.unc.edu (P.-T. Yap), dgshen@med.unc.edu (D. Shen).

https://doi.org/10.1016/j.media.2019.101540
1361-8415/

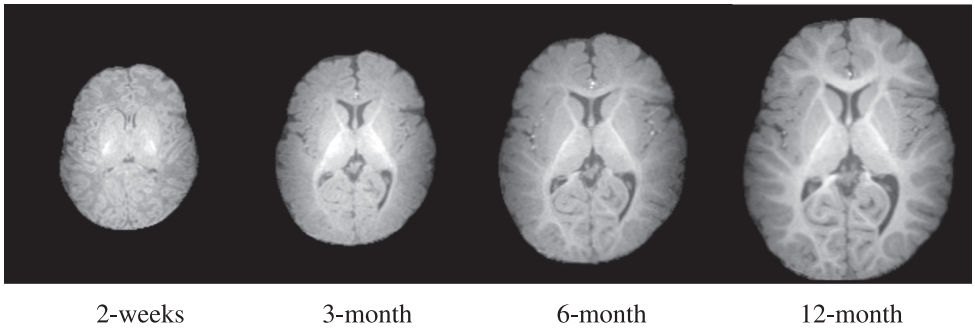

Fig. 1. Dynamic morphological and appearance changes in a typical infant brain from 2 weeks to 12 months of age demonstrated using T1-weighted MR images.

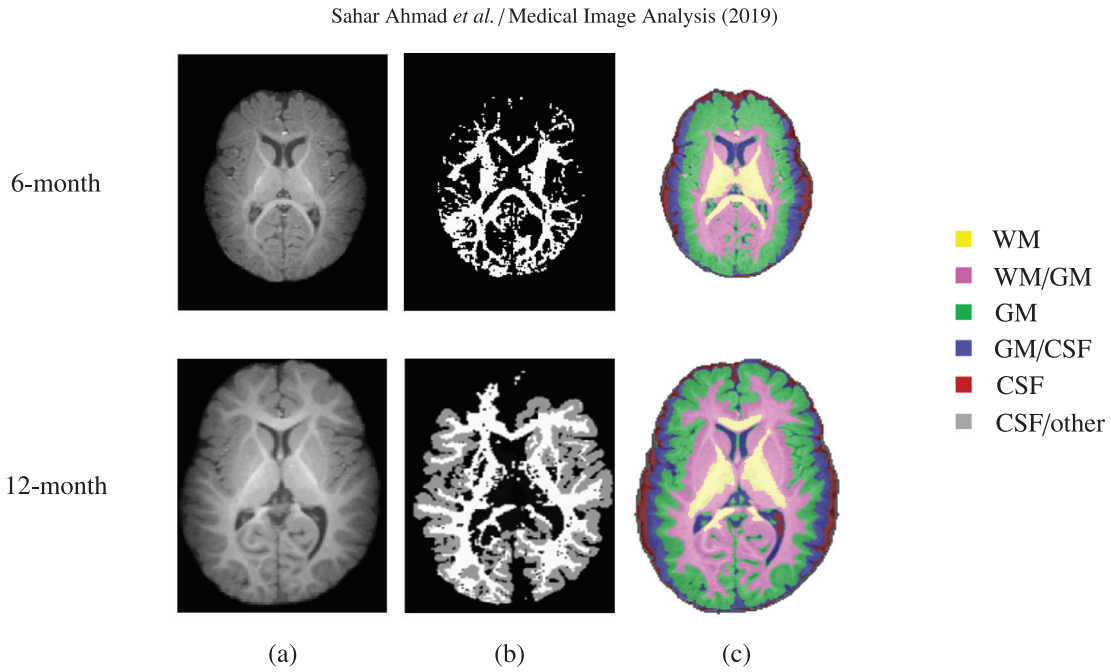

Fig. 2. Tissue segmentation of a typical 6-month-old (*first row*) and 12-month-old (*second row*). (a) T1-weighted MR brain image and segmentation results using (b) FreeSurfer and (c) BrainSuite.

Accurate volumetric registration does not necessarily guarantee accurate alignment of cortical surfaces (Park et al., 2012; Hellier et al., 2003). Cortical surfaces are highly convoluted with complex shapes and their alignment is important for studying cortical growth in early brain development (Li et al., 2014a). Surface-based registration methods (Park et al., 2012; Yeo et al., 2010; Zou et al., 2007; Joshi et al., 2012; Acosta et al., 2010) typically rely on information drawn from surface geometry (e.g., gyral and sulcal lines, sulcal depth, curvature, etc.). Although these methods provide accurate cortical surface correspondence, alignment of subcortical structures is totally ignored.

Combined surface and volumetric registration methods have emerged as a solution to the above limitations by concurrently aligning the cortical and subcortical structures. These methods not only work well for structural MRI, but have also shown efficacy in functional MRI (fMRI) registration (Gholipour et al., 2007) and improving alignment of fiber streamlines in diffusion MRI (dMRI) (Zöllei et al., 2010). This is typically achieved by reliably establishing correspondence across high-resolution structural MRI scans and then applying this to low-resolution fMRI or dMRI data. Surface-volume consistent infant brain atlases can also be constructed using combined surface and volume registration methods (Ahmad et al., 2019). While there are existing concurrent surface and volumetric registration methods (Postelnicu et al., 2009; Joshi et al., 2007), they are infeasible for infant brain images. The rapid appearance changes affect both segmentation and registration. For example, Fig. 2 indicates that the low contrast of T1-weighted MR brain image of 6-month-old and 12-month-old infant confuses FreeSurfer (Dale et al., 1999) and BrainSuite[1], resulting in tissue segmentation that cannot be used for surface reconstruction and registration.

[1] Available at http://brainsuite.org/processing/svreg/.

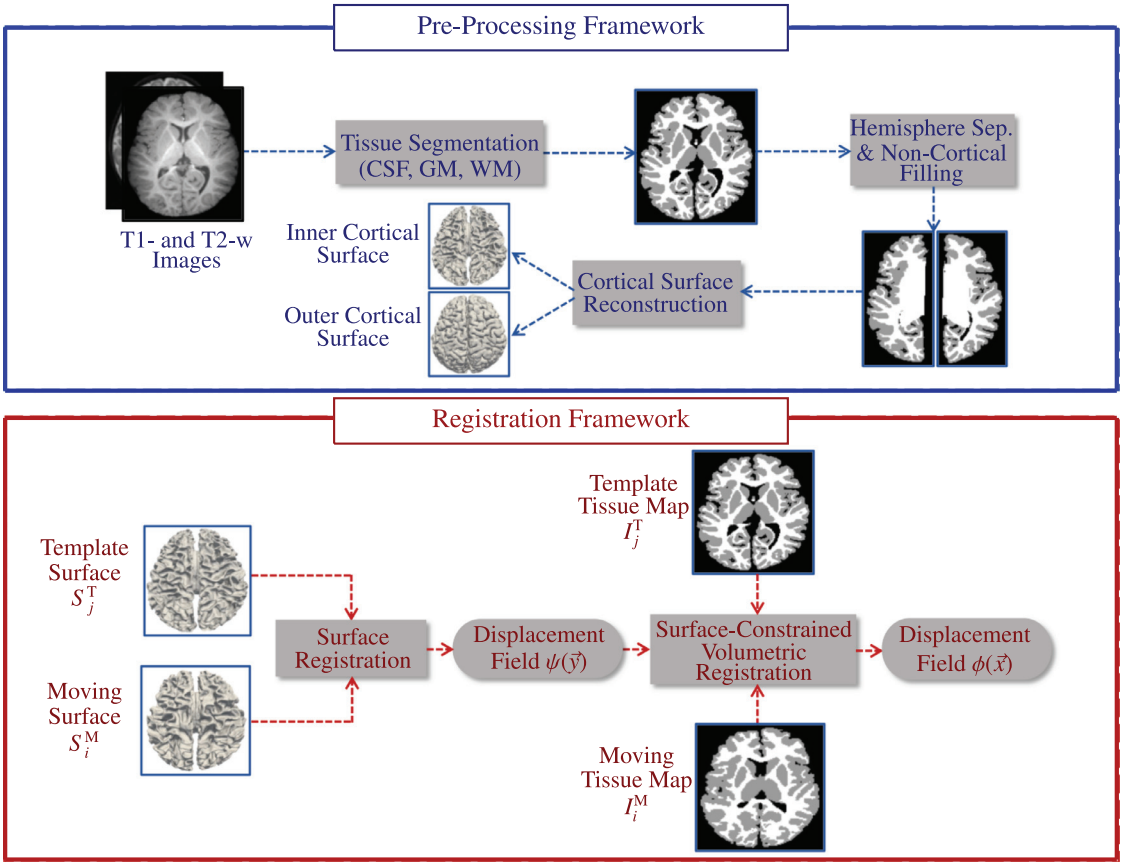

Fig. 3. Pipeline for surface-constrained volumetric registration.

In this paper, we introduce a surface-constrained volumetric registration method for infant brain MRI. The key steps involve (i) tissue segmentation using an infant-centric method developed by our group (Wang et al., 2015a); (ii) surface-based registration using cortical surfaces reconstructed based on the tissue segmentation outcome; and (iii) volumetric registration constrained by surface correspondences. We show that our method yields improvement in the alignment of cortical and subcortical structures over well-established registration methods.

The remainder of the paper is organized as follows. In Section 2, we present the dataset used in this study. In Section 3, we describe the proposed registration method. In Section 4, we show evaluation results for inter- and intra-subject registration. Finally, we conclude the paper in Section 5.

2. Materials

An infant brain MRI dataset consisting of images acquired for 19 healthy infant subjects (males: 14, females: 5) was used to validate the performance of the proposed method. T1- and T2-weighted MR images of each subject were scanned at 2 weeks, 3 months, 6 months and 12 months. The imaging parameters for T1-weighted MR images were TR = 1900 ms, TE = 4.38 ms, flip angle = 7°, 144 sagittal slices and 1 mm isotropic voxel size. The imaging parameters for T2-weighted MR images were TR = 7380 ms, TE = 119 ms, flip angle = 150°, 64 sagittal slices, and $1.25 \times 1.25 \times 1.95\,\text{mm}^3$ voxel size.

3. Methods

We present a surface-constrained volumetric registration method with the goal of aligning a moving image I_i^M at time point i and template image I_j^T at time point j. Due to significant appearance changes, registration cannot be performed directly on the intensity images. As an alternative, we register the tissue maps generated using our infant-centric segmentation method (Wang et al., 2015a). Therefore, I_i^M and I_j^T are tissue maps instead of intensity images, making the registration process insensitive to contrast changes. Fig. 3 shows the complete pipeline of the proposed technique, consisting of (i) data pre-processing for obtaining tissue maps and cortical surfaces, and (ii) surface-constrained non-linear volumetric registration.

3.1. Pre-processing framework

The longitudinally acquired infant images were processed using the UNC infant cortical surface processing pipeline (Li et al., 2014a, 2013, 2015b, 2014c), which includes: (i) N3 intensity inhomogeneity correction (Sled et al., 1998); (ii) skull stripping by a learning-based method (Shi et al., 2012); (iii) cerebellum and brain stem removal by registration (Shen and Davatzikos, 2002); (iv) rigid alignment of all longitudinal images of the same subject and rigid alignment of T2-weighted images with the corresponding T1-weighted images; (v) longitudinally consistent tissue segmentation (CSF, GM and WM) using a learning-based multi-source integration framework (Wang et al., 2015a); (vi) masking and filling of non-cortical

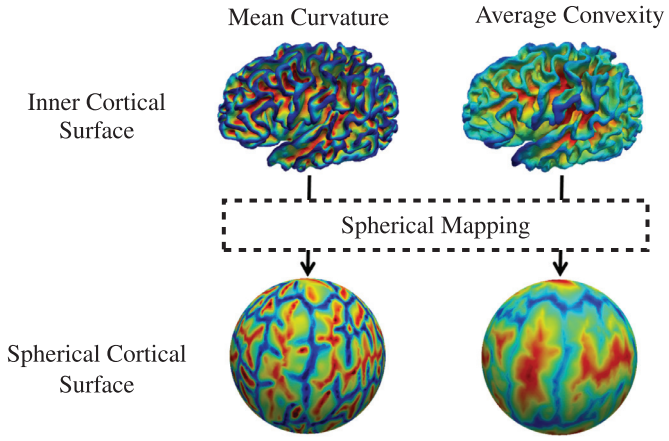

Fig. 4. Spherical mapping of the inner cortical surface.

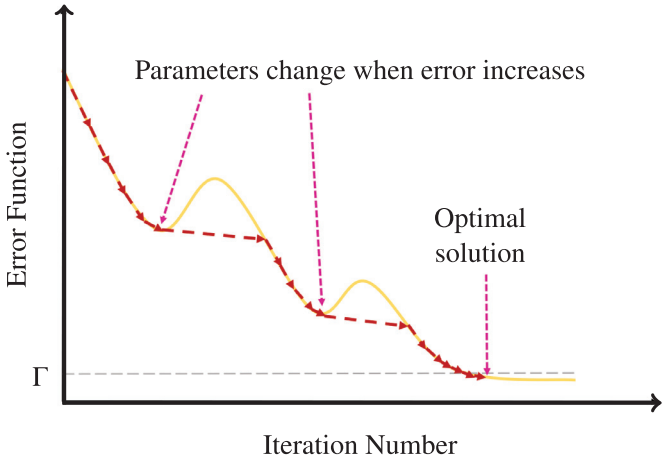

Fig. 5. Illustration of optimization procedure.

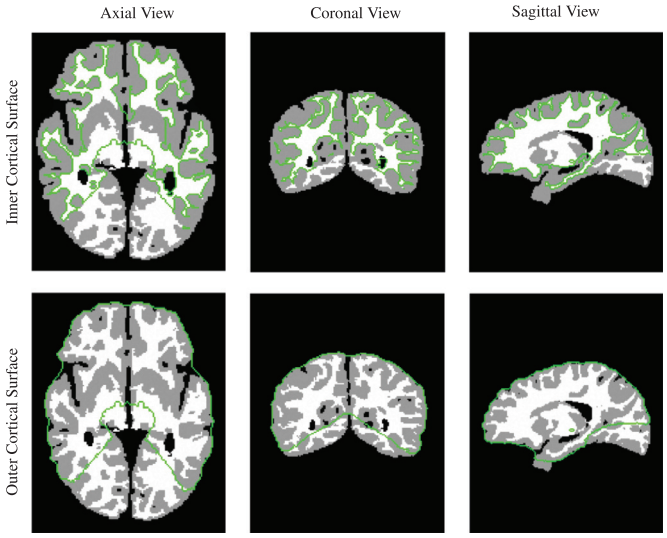

Fig. 6. Inner and outer cortical surfaces generated by BrainSuite.

structures and separation of each brain into left and right hemispheres (Li et al., 2013, 2014b); (vii) construction of topologically correct and geometrically accurate inner (WM-GM interface) and outer (GM-CSF interface) cortical surfaces (Li et al., 2014a, 2012).

3.2. Registration framework

The registration framework begins with cortical surface registration, followed by surface-guided volumetric registration.

3.2.1. Cortical surface registration

The cortical surfaces (left/right, inner/outer) of the moving subject S_i^{M} at time point i are registered to the corresponding cortical surfaces of the template S_j^{T} at time point j, thus aligning cortical folds. In order to simplify cortical surface registration, spherical mapping is performed by inflating the inner cortical surface and mapping the outcome onto a sphere (Fig. 4) by minimizing the metric distortion between the original cortical surface and its spherical representation (Fischl et al., 1999). We first use Spherical Demons (Yeo et al., 2010) to align the spherical cortical surfaces in a pairwise manner. The registration is driven by two commonly used folding attributes, i.e., average convexity and mean curvature (Fischl et al., 1999). The vertex-to-vertex correspondences established by spherical registration are then propagated to the inner and outer cortical surfaces by leveraging the one-to-one vertex mapping between the spherical representation and, the inner and outer cortical surfaces. Finally, based on the correspondences between cortical surfaces, we obtain the displacement $\psi(\vec{y})$ for each vertex $\vec{y} = (y_1, y_2, y_3)$ of the template cortical surface with respect to the moving surface. This displacement field will be used to constrain subsequent volumetric registration, as detailed below.

3.2.2. Surface-constrained volumetric registration

Cortical and subcortical structures can be consistently aligned by constraining the volumetric registration with the displacement obtained by cortical surface registration. The deformation is defined as $\mathcal{T}(\vec{x}) = \vec{x} + \phi(\vec{x}),\ \vec{x} \in \Omega$, where $\phi : \Omega \to \mathbb{R}^3$ is a displacement field defined on the brain region $\Omega \subset \mathbb{R}^3$ and $\vec{x}$ denotes the 3D spatial coordinates. Here, our objective is to seek an optimal displacement such that $\phi(\vec{y}) = \psi(\vec{y})$, for every vertex $\vec{y}$ of S_j^{T}. We use the dynamic elasticity model (DEM) (Ahmad and Khan, 2017) to represent the underlying large non-linear displacement. DEM registration is formulated based on the principle of elastodynamics dealing with dynamic displacements. The image is modeled as an elastic body that is disturbed from its resting state by an abrupt external force. This disturbance takes the form of elastic waves propagating across the entire body. These elastic waves characterize the non-linear displacements, which can be recovered using the elastodynamics wave equation given as:

$$\frac{\partial^2 \phi(\vec{x})}{\partial t^2} = \alpha\left(\nabla^2 \phi(\vec{x}) + \nabla(\nabla \cdot \phi(\vec{x}))\right) + \beta f^{\mathrm{V}}(\vec{x}), \tag{1}$$

where parameter α influences the smoothness of the displacement field and β controls the contribution of the volumetric force field $f^{\mathrm{V}}(\vec{x})$, which is computed as the gradient of the L^2 distance between $I_i^{\mathrm{M}}(\mathcal{T}(\vec{x}))$ and $I_j^{\mathrm{T}}(\vec{x})$, i.e.,

$$E^{\mathrm{V}}(\vec{x}) = \frac{1}{2}\int_{\Omega} \left| I_i^{\mathrm{M}}(\mathcal{T}(\vec{x})) - I_j^{\mathrm{T}}(\vec{x}) \right|^2 d\vec{x}, \tag{2}$$

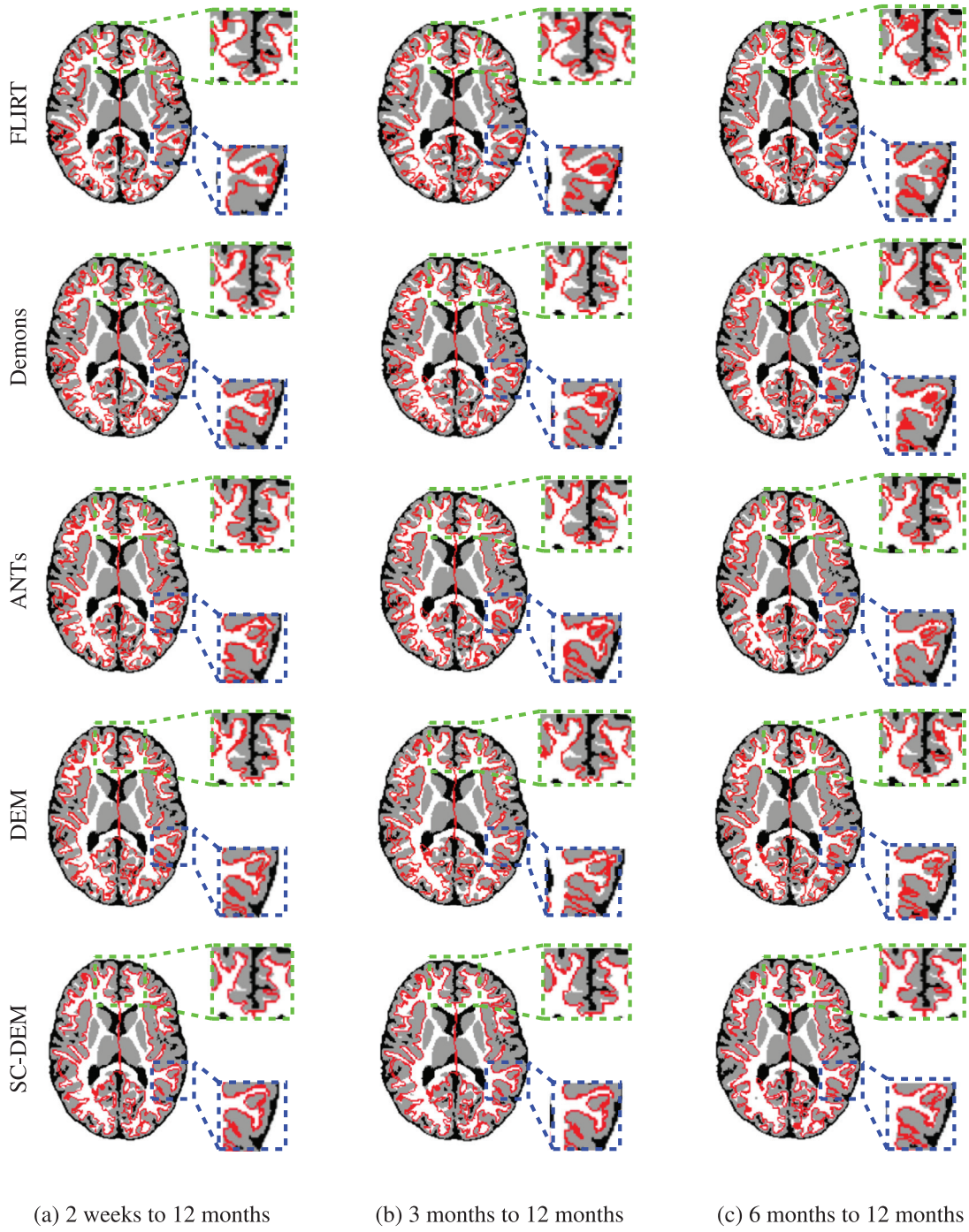

Fig. 7. Inner cortical surface of the moving image warped using FLIRT (*first row*), diffeomorphic Demons (*second row*), ANTs (*third row*), DEM (*fourth row*) and SC-DEM (*fifth row*) overlaid on the template tissue map used in inter-subject registration.

given as

$$f^{\mathrm{V}}(\vec{x}) = \frac{\partial E^{\mathrm{V}}(\vec{x})}{\partial \mathcal{T}} = -\left[I_i^{\mathrm{M}}(\mathcal{T}(\vec{x})) - I_j^{\mathrm{T}}(\vec{x})\right] \frac{\partial I_i^{\mathrm{M}}(\mathcal{T}(\vec{x}))}{\partial \mathcal{T}} \tag{3}$$

Volumetric registration is steered by $f^{\mathrm{V}}(\vec{x})$, which is influenced by two terms as given in Eq. (3). The first term (within square brackets) defines the discrepancy between the template and the moving tissue map warped using the estimated deformation field. The second term is the gradient of the warped moving tissue map. Voxels associated with high gradient magnitudes are structural edges that drive the registration. The volumetric force field diminishes with the alignment of template and moving tissue maps. When the force is close to zero, the displacement field converges with no further significant changes.

Here, we incorporate the cortical surface constraint into Eq. (1) by defining a surface force field $f^{\mathrm{S}}(\vec{y})$, computed as the difference between the displacements estimated respectively from

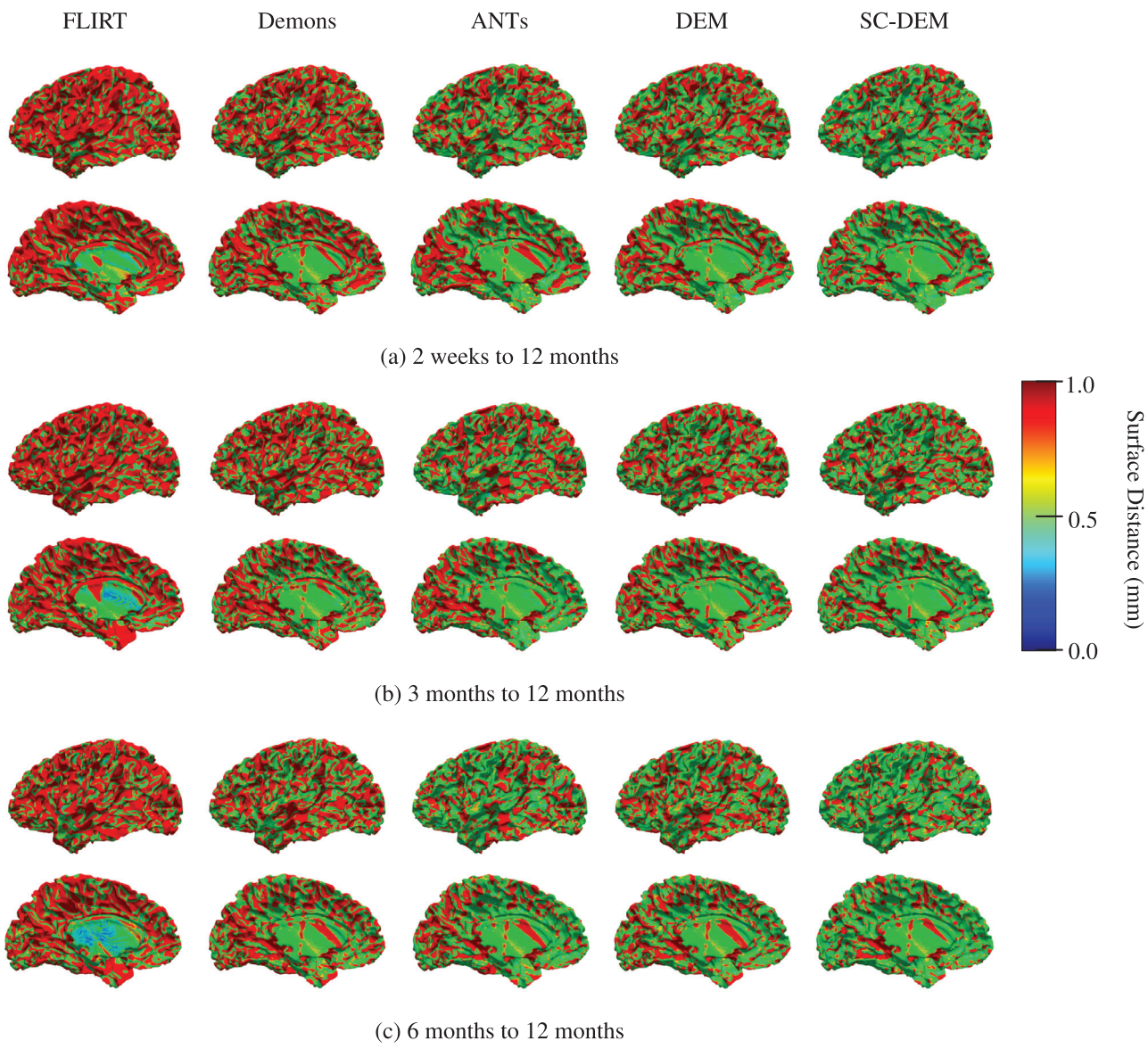

Fig. 8. Cortical surface distance between the template cortical surface and the moving cortical surface warped using FLIRT (*first column*), diffeomorphic Demons (*second column*), ANTs (*third column*), DEM (*fourth column*) and SC-DEM (*fifth column*) for inter-subject registration.

surface and volumetric registration:

$$f^{S}(\vec{y}) = \psi(\vec{y}) - \phi(\vec{y}) \tag{4}$$

Accordingly, the elastodynamics wave equation is modified as

$$\frac{\partial^2 \phi(\vec{x})}{\partial t^2} = \alpha\left(\nabla^2\phi(\vec{x}) + \nabla(\nabla\cdot\phi(\vec{x}))\right) + \beta f^{V}(\vec{x}) + \gamma f^{S}(\vec{x}), \tag{5}$$

where the parameter γ controls the contribution of the surface force. The modified elastodynamics wave equation is governed by two forces i.e., volumetric and surface force fields. These force fields reflect the misalignment between a pair of tissue maps and the corresponding cortical surfaces. The magnitudes of these force fields are initially high but diminish with alignment, resulting in the convergence of the displacement field. The surface-constrained dynamic elasticity model (SC-DEM) based registration algorithm is described below:

Step 1: Initialize the displacement fields for the first two iterations (i.e., $t = 0$ and $t = 1$) with zero:

$$\phi_0(\vec{x}) = \phi_1(\vec{x}) = 0$$

Step 2: Estimate the displacement $\phi_t(\vec{y})$ at vertices of the template cortical surface:

$$\phi_t(\vec{x}) \xrightarrow{\text{interpolation}} \phi_t(\vec{y})$$

Step 3: Deform $I_i^{M}(\vec{x})$ with the current estimated deformation $\mathcal{T}_t(\vec{x})$ and compute the volumetric force field $f_t^{V}(\vec{x})$ using Eq. (3).

Step 4: Calculate the surface force field by extrapolating the difference between $\psi(\vec{y})$ and $\phi_t(\vec{y})$ over the entire volumetric space:

$$f_t^{S}(\vec{y}) \xrightarrow{\text{extrapolation}} f_t^{S}(\vec{x})$$

Table 1
Statistical summary (mean ± std) of whole-brain Dice ratio (%) for inter-subject registration. Best results are shown in bold and "*" indicates $p < 0.01$ for paired t-test.

Method	2 weeks to 12 months	3 months to 12 months	6 months to 12 months
FLIRT	$52.51 \pm 1.05^*$	$53.21 \pm 1.03^*$	$54.93 \pm 1.23^*$
Demons	$69.71 \pm 0.55^*$	$70.16 \pm 0.54^*$	$71.59 \pm 0.40^*$
ANTs	$74.37 \pm 0.73^*$	$74.95 \pm 0.74^*$	$76.43 \pm 0.57^*$
DEM	$75.36 \pm 0.69^*$	$75.02 \pm 0.53^*$	$76.44 \pm 0.53^*$
SC-DEM	$\mathbf{80.57 \pm 0.88}$	$\mathbf{81.71 \pm 0.82}$	$\mathbf{82.94 \pm 0.54}$

Table 2
List of 34 cortical ROIs.

ID	ROI	ID	ROI
1	Caudal Middle Frontal	18	Rostral Middle Frontal
2	Entorhinal	19	Rostral Anterior Cingulate
3	Post Central	20	Isthmus Cingulate
4	Pars Triangularis	21	Lateral Occipital
5	Supra Marginal	22	Lingual
6	Isthmus Insula	23	Superior Parietal
7	Banks Superior Temporal	24	Pars Opercularis
8	Lateral Orbito Frontal	25	Fusiform
9	Pars Orbitalis	26	Caudal Anterior Frontal
10	Middle Temporal	27	Superior Frontal
11	Peri Calcarine	28	Temporal Pole
12	Parahippocampal	29	Pre Cuneus
13	Para Central	30	Transverse Temporal
14	Medial Orbital Frontal	31	Pre Central
15	Frontal Pole	32	Inferior Parietal
16	Cuneus	33	Posterior Cingulate
17	Inferior Temporal	34	Superior Temporal

Step 5: $f_t^V(\vec{x})$ and $f_t^S(\vec{x})$ are then combined and convolved with a Gaussian kernel of size $3 \times 3 \times 3$ and $\sigma^2 = 0.8$ to obtain the combined force field as follows:

$$f_t^C(\vec{x}) = G_{\sigma^2} \circledast \left(\beta f_t^V(\vec{x}) + \gamma f_t^S(\vec{x})\right) \tag{6}$$

Step 6: If $|\bar{f}_t^C| > \Gamma$, where $\bar{f}_t^C$ is the mean of $f_t^C(\vec{x})$ and Γ is a threshold, then the displacement field for the next iteration is computed using

$$\begin{aligned}\phi_{t+1}(\vec{x}) = \alpha\left(\nabla^2\phi_t(\vec{x}) + \nabla(\nabla \cdot \phi_t(\vec{x}))\right) \\ + f_t^C(\vec{x}) + 2\phi_t(\vec{x}) - \phi_{t-1}(\vec{x})\end{aligned} \tag{7}$$

Step 7: Compute surface displacement error $E_t^S(\vec{y})$ as follows:

$$E_t^S(\vec{y}) = \sqrt{(\psi(y_1) - \phi_t(y_1))^2 + (\psi(y_2) - \phi_t(y_2))^2 + (\psi(y_3) - \phi_t(y_3))^2}$$

Step 8: Increment β with step size $\Delta\beta$. Repeat Steps 2 – 7 until either median$(E_t^S(\vec{y})) >$ median$(E_{t-1}^S(\vec{y}))$ or $|\bar{f}_t^C| < \Gamma$. Proceed to the next level as soon as one of the conditions is met.

Step 9: At the next level, initialize $\phi_t(\vec{x})$ with $\phi_{t-1}(\vec{x})$, decrement α and increment γ with step size $\Delta\alpha$ and $\Delta\gamma$, respectively.

Step 10: Loop over Steps 2 - 9 until the highest level is reached. Warp I_i^M with final estimated deformation to obtain aligned moving tissue map.

The optimal displacement is obtained by formulating image registration as a wave motion problem. The moving tissue map is deformed toward the template tissue map by the minimization of an energy functional given by tissue map dissimilarity and surface displacement error. If during minimization, the error gets worse (Step 8, median$(E_t^S(\vec{y})) >$ median$(E_{t-1}^S(\vec{y}))$), then the change in parameter settings allows further minimization of the error. Thus, the proposed multi-level registration strategy avoids local minima and recovers residual displacements, improving the registration quality (Fig. 5). The second condition in Step 8 ($|\bar{f}_t^C| < \Gamma$) guarantees sufficient minimization of the error function, such that the algorithm converges. This condition also prevents estimation of excessive deformations that may cause the algorithm to oscillate near convergence. In practice, we observed that the algorithm converges to a reasonable solution within 20 iterations with $\Gamma = 1 \times 10^{-5}$.

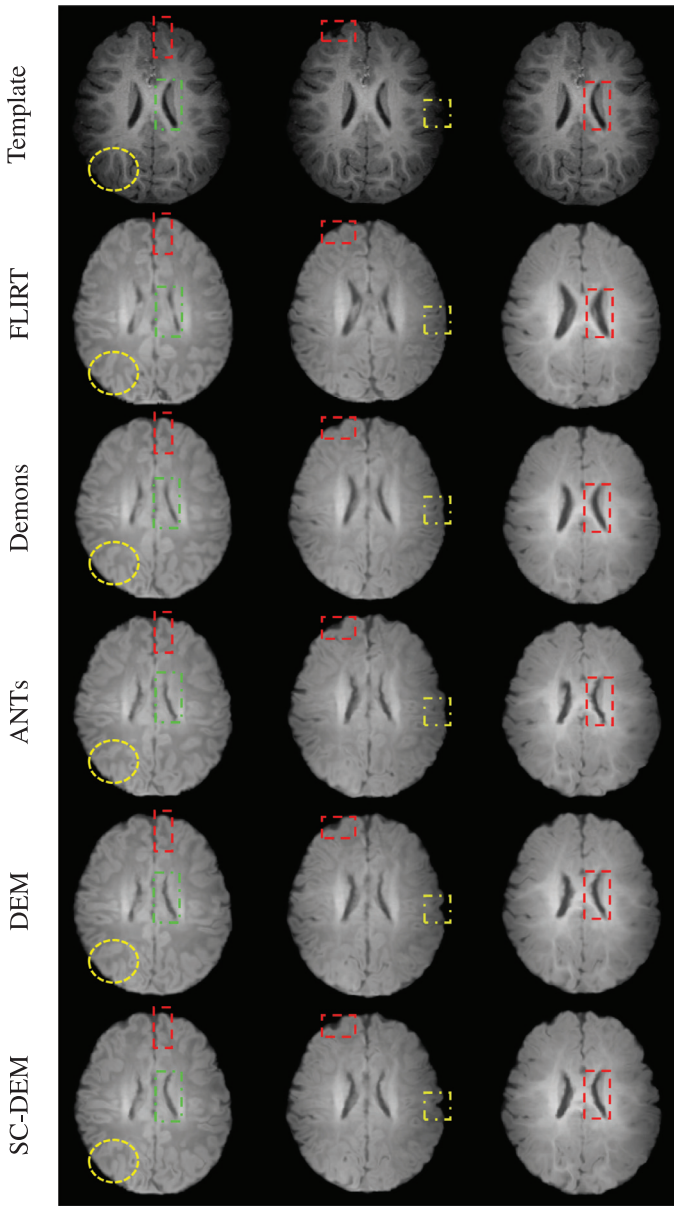

(a) 2 weeks to 12 months (b) 3 months to 12 months (c) 6 months to 12 months

Fig. 9. Moving T1-weighted image warped using FLIRT (*second row*), diffeomorphic Demons (*third row*), ANTs (*fourth row*), DEM (*fifth row*) and SC-DEM (*sixth row*), in comparison with the template image (*first row*) used in inter-subject registration.

Table 3
Statistical summary (mean ± std) of modified Hausdorff distance (mm) for inter-subject registration. Best results are shown in bold and "*" indicates $p < 0.01$ for paired t-test.

Method	2 weeks to 12 months		3 months to 12 months		6 months to 12 months	
	Inner Cortical Surface	Outer Cortical Surface	Inner Cortical Surface	Outer Cortical Surface	Inner Cortical Surface	Outer Cortical Surface
FLIRT	1.49 ± 0.05*	1.91 ± 0.08*	1.44 ± 0.05*	1.82 ± 0.08*	1.37 ± 0.05*	1.71 ± 0.08*
Demons	1.14 ± 0.03*	1.33 ± 0.04*	1.15 ± 0.04*	1.35 ± 0.04*	1.12 ± 0.03*	1.28 ± 0.04*
ANTs	0.96 ± 0.04*	1.12 ± 0.05*	0.96 ± 0.04*	1.13 ± 0.05*	0.94 ± 0.03*	1.08 ± 0.04*
DEM	0.92 ± 0.04*	1.05 ± 0.05*	0.95 ± 0.03*	1.10 ± 0.03*	0.95 ± 0.04*	1.07 ± 0.04*
SC-DEM	**0.79 ± 0.02**	**0.92 ± 0.03**	**0.78 ± 0.02**	**0.91 ± 0.03**	**0.79 ± 0.03**	**0.89 ± 0.03**

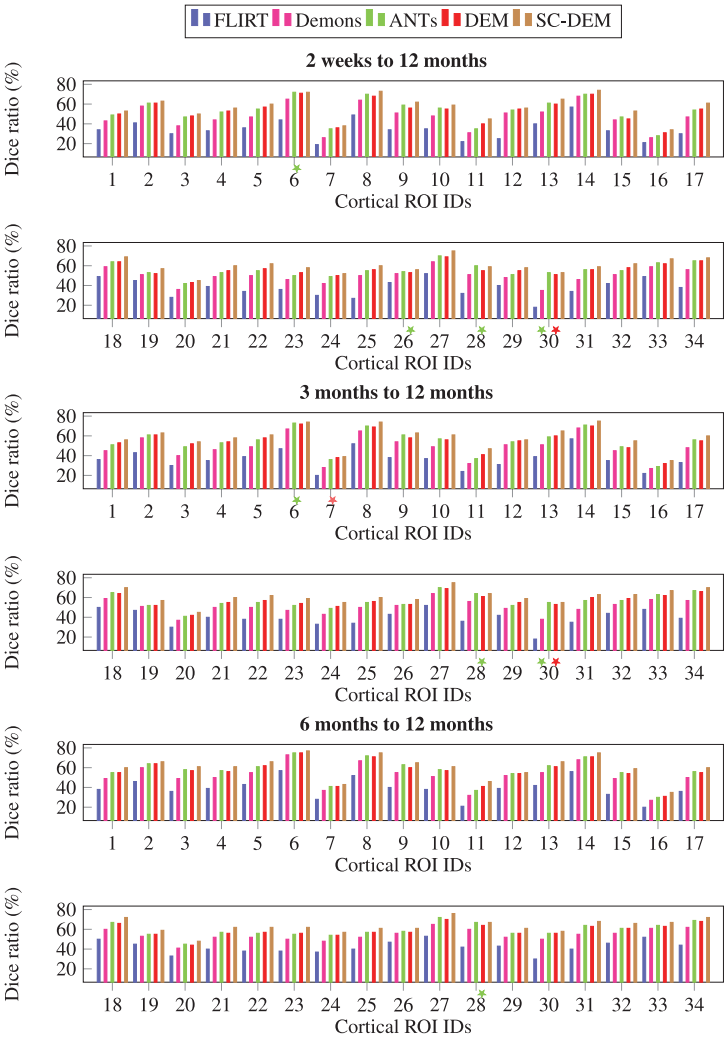

Fig. 10. Inter-subject registration results in terms of Dice ratio for cortical ROIs. The colored stars mark differences that are not statistically significant ($p > .01$) with reference to SC-DEM.

Table 4
Statistical summary (mean ± std) of whole-brain Dice ratio (%) for intra-subject registration. Best results are shown in bold and "*" indicates $p < 0.01$ for paired t-test.

Method	2 weeks to 12 months	3 months to 12 months	6 months to 12 months
FLIRT	57.74 ± 2.57*	63.98 ± 3.85*	76.12 ± 2.01*
Demons	79.33 ± 1.78*	81.86 ± 1.62*	84.98 ± 0.70*
ANTs	82.83 ± 0.99*	84.03 ± 0.73*	85.45 ± 0.73*
DEM	81.83 ± 1.15*	83.53 ± 1.03*	86.29 ± 0.94*
SC-DEM	**86.28 ± 1.14**	**86.64 ± 1.33**	**88.45 ± 0.78**

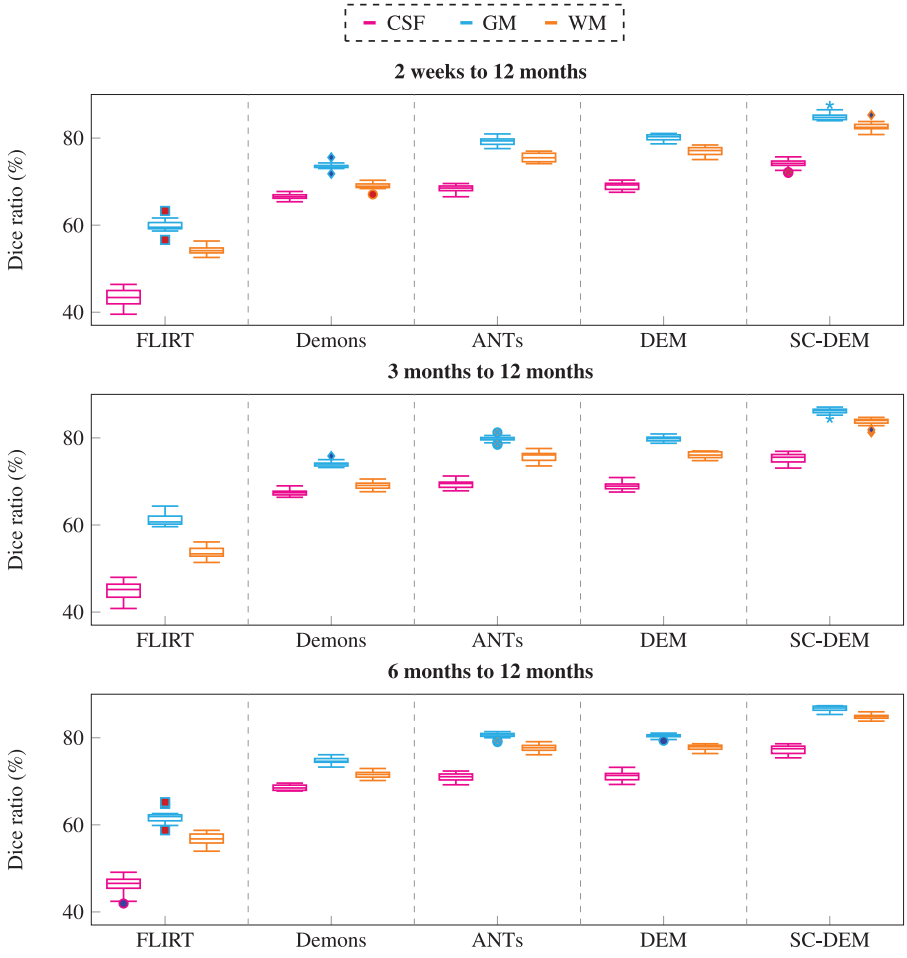

Fig. 11. Inter-subject registration results in terms of Dice ratio for different tissue types (CSF, GM, WM).

Table 5
Statistical summary (mean ± std) of modified Hausdorff distance (mm) for intra-subject registration. Best results are shown in bold and "*" indicates $p < 0.01$ for paired t-test.

Method	2 weeks to 12 months		3 months to 12 months		6 months to 12 months	
	Inner Cortical Surface	Outer Cortical Surface	Inner Cortical Surface	Outer Cortical Surface	Inner Cortical Surface	Outer Cortical Surface
FLIRT	$1.33 \pm 0.10^*$	$1.75 \pm 0.18^*$	$1.13 \pm 0.14^*$	$1.40 \pm 0.26^*$	$0.67 \pm 0.08^*$	$0.75 \pm 0.10^*$
Demons	$0.75 \pm 0.09^*$	$0.86 \pm 0.10^*$	$0.70 \pm 0.09^*$	$0.81 \pm 0.11^*$	$0.63 \pm 0.04^*$	$0.71 \pm 0.05^*$
ANTs	$0.62 \pm 0.03^*$	$0.71 \pm 0.05^*$	$0.63 \pm 0.03^*$	$0.72 \pm 0.05^*$	$0.63 \pm 0.03^*$	$0.71 \pm 0.04^*$
DEM	0.61 ± 0.02	$0.71 \pm 0.03^*$	0.61 ± 0.04	0.71 ± 0.05	0.59 ± 0.04	$0.68 \pm 0.04^*$
SC-DEM	$\mathbf{0.56 \pm 0.03}$	$\mathbf{0.66 \pm 0.04}$	$\mathbf{0.59 \pm 0.05}$	$\mathbf{0.69 \pm 0.07}$	$\mathbf{0.58 \pm 0.03}$	$\mathbf{0.66 \pm 0.04}$

3.3. Implementation details

Here, we describe the implementation details of SC-DEM. In Step 2, we use trilinear interpolation to estimate the value of displacement at surface vertices (non-grid points) from the displacement field of image voxels (grid points). In Step 4, the surface force field is extrapolated over the volumetric space using Delaunay triangulation to generate the mesh and then the mesh vertices are displaced by distance specified as the magnitude of surface force field. In order to determine the value of force field at a particular voxel, first the triangulation data structure is traversed to find the triangle that encloses the given voxel. Then, the value at voxel is determined by the weighted sum of the values associated with the enclosing triangle vertices and the corresponding weights are pre-computed using barycentric coordinates.

In Eq. (6), the values of parameters β and γ are tweaked to balance the volumetric and surface force fields. Initially, the value of β is set to 1.1, which is iteratively incremented with $\Delta\beta = 0.012$. γ is defined as a spatially varying parameter, i.e., its value is initialized with 2×10^{-4} for the voxels representing cortical region and zero for all other voxels. With this, the alignment of cortical region is driven by both volumetric and surface force fields, whereas

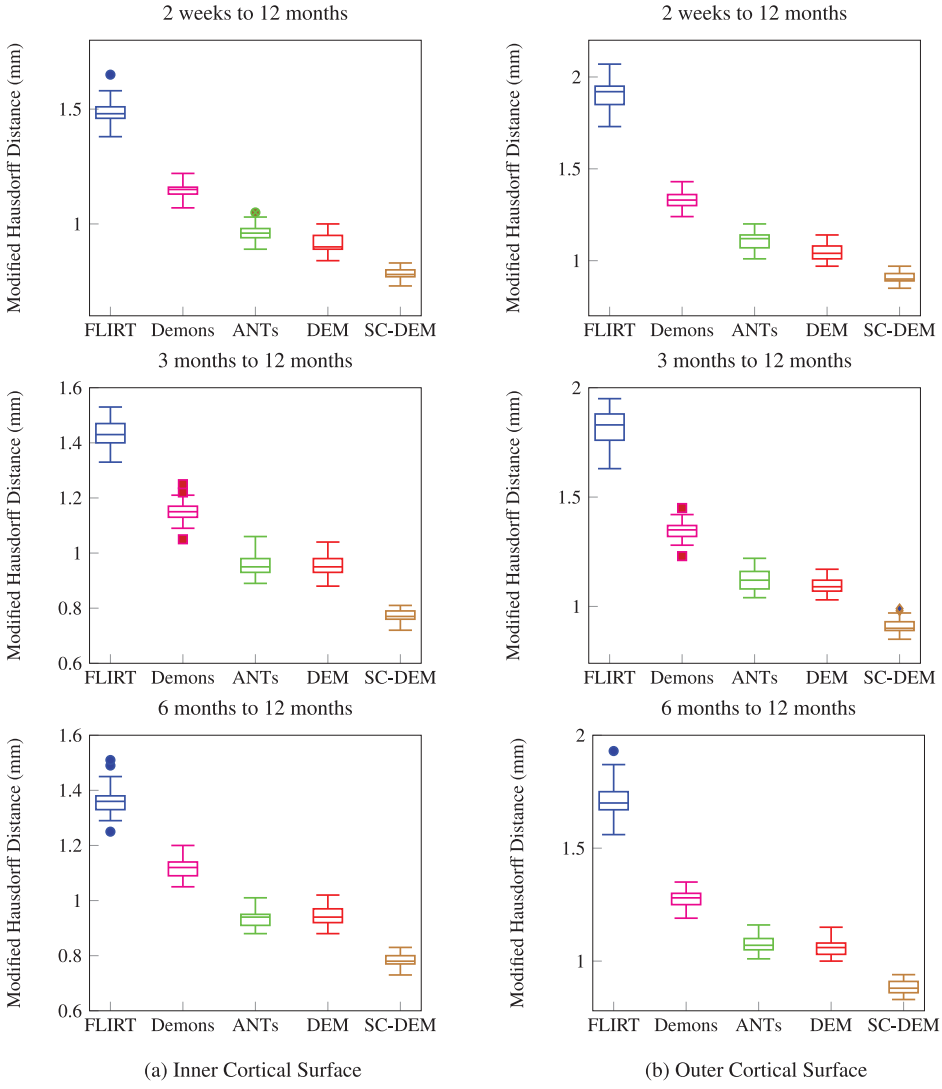

Fig. 12. Inter-subject registration results in terms of modified Hausdorff distance for inner and outer cortical surfaces.

the subcortical region is aligned under the influence of volumetric force field. In Step 9, γ is incremented for cortical voxels with $\Delta\gamma = 2 \times 10^{-4}$. These values were empirically chosen such that the two forces are of the same order.

The regularization constant α in Eq. (7) is also defined as a spatially varying parameter, i.e., the voxels representing different tissue types have different values. We set the value in accordance with the mechanical properties of the tissues. According to (Budday et al., 2015), WM is more rigid than GM due to the presence of myelinated axons in WM. Thus, in view of the elastic properties of WM and GM, WM voxels are assigned lower value than GM voxels as follows:

$$\alpha = \begin{cases} 0.16 & \text{if } \vec{x} \in \text{WM} \\ 0.18 & \text{if } \vec{x} \in \text{GM} \\ 0.22 & \text{otherwise.} \end{cases} \tag{8}$$

The heterogeneous α ensures that the different brain tissues deform at the same rate and the estimated displacement field is smooth. Otherwise, the displacement field would be under-regularized if α is kept small for all the tissues. On the other hand, a higher value would result in an over-regularized displacement field. At each level, the value of α is decremented for GM and WM voxels with a step size $\Delta\alpha = 0.006$. This allows the recovery of residual local displacements. α is kept constant once it drops to 0.06. If we keep on decreasing α beyond 0.06, then the tissue map would undergo excessive displacement, resulting in an irregular displacement field. Lastly, Eq. (7) is solved using finite difference approximation.

The parameter setting is in general insensitive to the type of dataset used as we do not work directly with the intensity images but rather the tissue maps, provided tissue segmentation can be performed reliably.

4. Results and discussion

4.1. Inter-subject registration

We registered the tissue maps of all subjects at 2 weeks, 3 months and 6 months to a 12 month template tissue map. The tissue map of a 12-month subject with the minimum median dissimilarity with the tissue maps of all other 12-month subjects was selected as the template in order to reduce potential

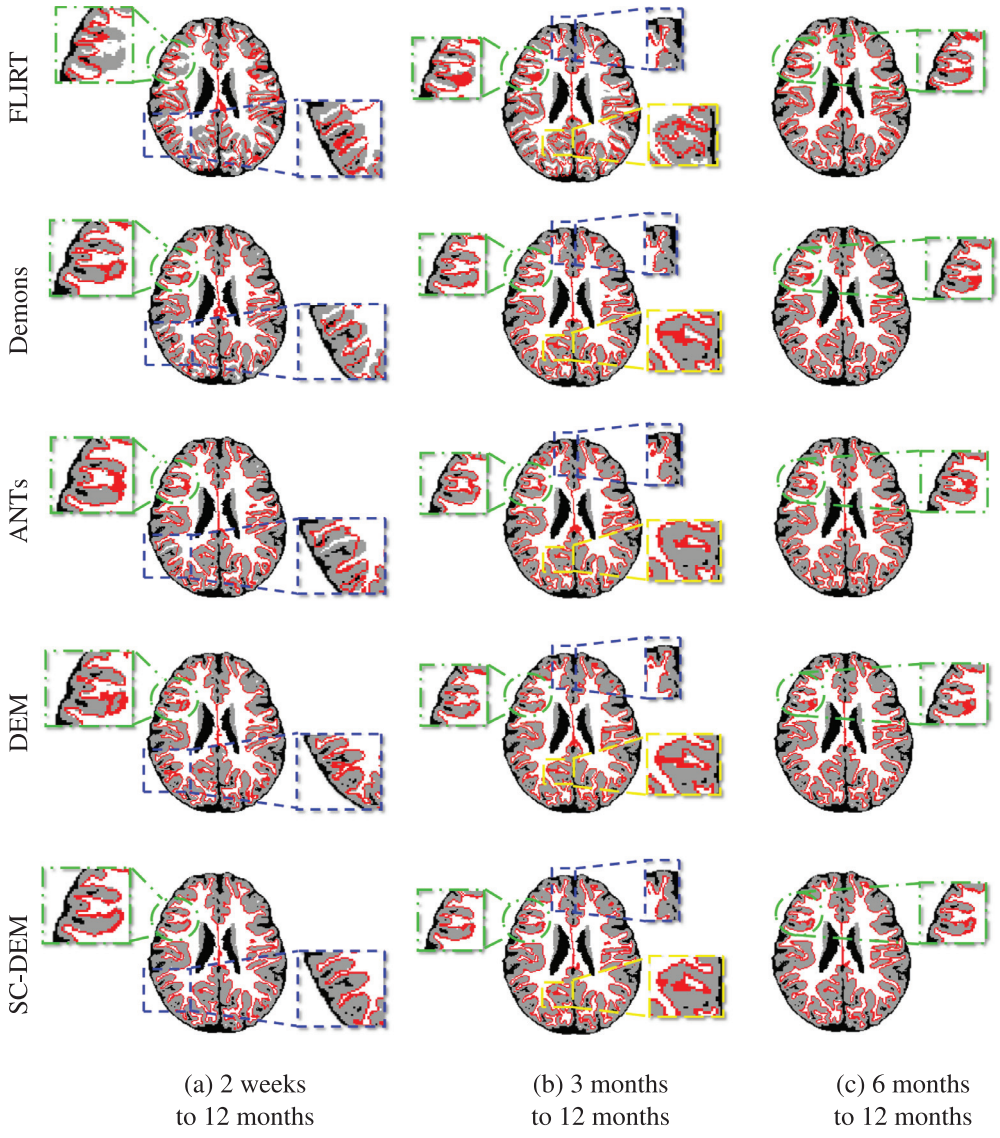

Fig. 13. Inner cortical surface of the moving image warped using FLIRT (*first row*), diffeomorphic Demons (*second row*), ANTs (*third row*), DEM (*fourth row*) and SC-DEM (*fifth row*) overlaid on the template tissue map for intra-subject registration.

bias associated with template selection. All moving tissue maps, T1-weighted MR images and cortical surfaces were affinely registered to the template using FLIRT (Jenkinson and Smith, 2001; Jenkinson et al., 2002). We compared the performance of SC-DEM with state-of-the-art registration methods, including diffeomorphic Demons (Vercauteren et al., 2009), ANTs (Avants et al., 2008) and DEM (Ahmad and Khan, 2017). For all methods, registration was based on tissue maps instead of intensity images. We did not compare our method with existing surface-constrained registration methods because they give unsatisfactory segmentation results (Fig. 2), negatively affecting subsequent surface and volumetric registration. The cortical surfaces generated by BrainSuite using our tissue maps are inaccurate (see Fig. 6) and hence cannot be used for surface-constrained registration. No option was provided to use our own cortical surface for registration.

Table 6
Parameters range.

β	γ	α_{WM}	α_{GM}	α_{other}
[0.10,3.00]	[0.0001,0.003]	[0.14,0.18]	[0.16,0.20]	[0.20,0.25]

4.1.1. Qualitative evaluation

We qualitatively evaluated the registration performance using multiple criteria. First, we visually inspected the alignment of cortical surface reconstructed from the warped moving tissue map. Fig. 7 shows the warped inner cortical surface given by five different methods for registration from 2 weeks to 12 months (Fig. 7(a)), 3 months to 12 months (Fig. 7(b)), and 6 months to 12 months (Fig. 7(c)). As indicated by the zoomed-in views of the dashed

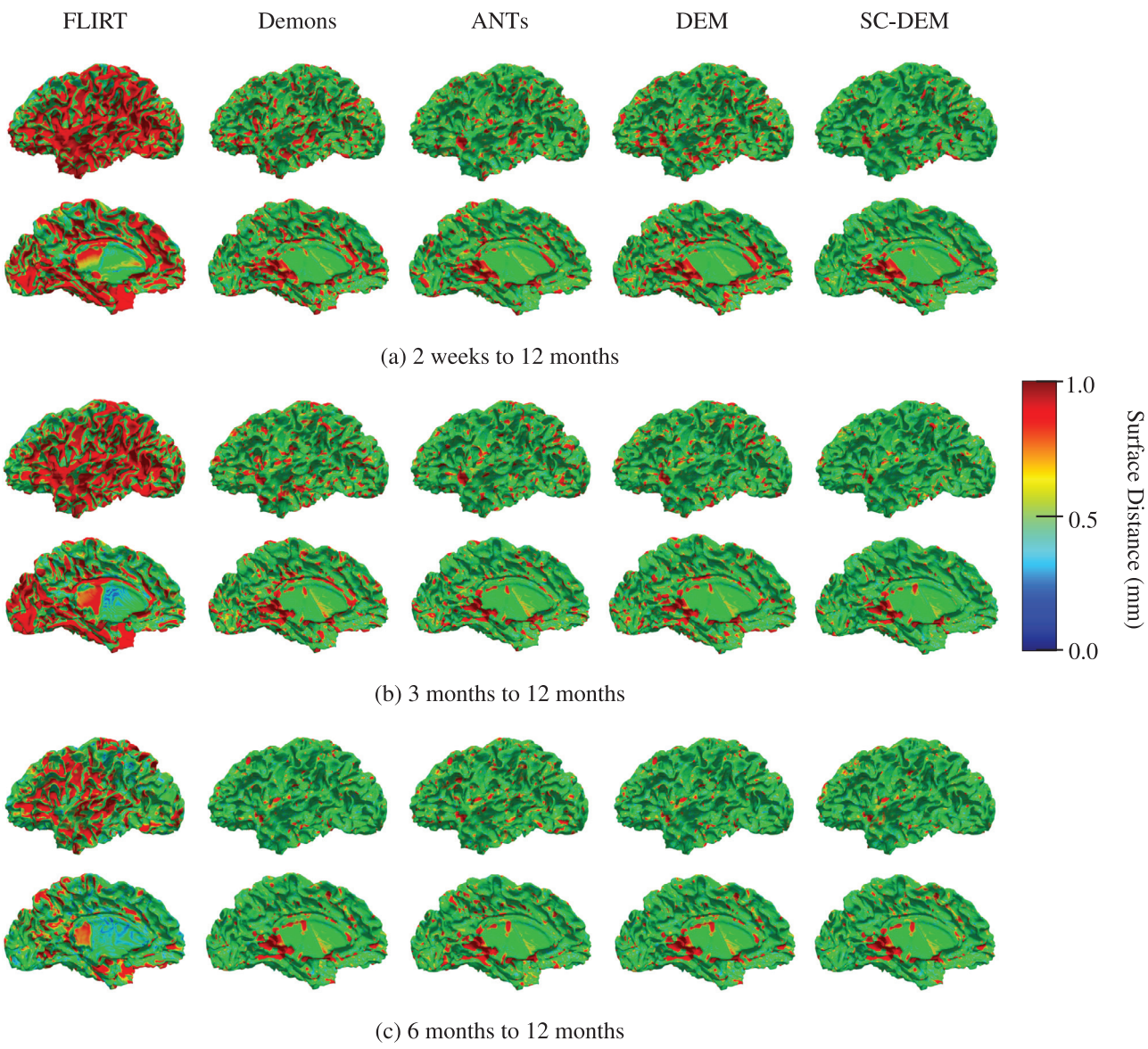

Fig. 14. Cortical surface distance between the template cortical surface and the moving cortical surface warped using FLIRT (*first column*), diffeomorphic Demons (*second column*), ANTs (*third column*), DEM (*fourth column*) and SC-DEM (*fifth column*) for intra-subject registration.

boxes, SC-DEM achieves good alignment of the cortical surfaces with the tissue maps. Fig. 8(a–c) shows the surface distance (computed using Hausdorff metric) between the warped moving cortical surface and the template cortical surface for registration from 2 weeks, 3 months, and 6 months to 12 months, respectively. It can be seen that SC-DEM yields smaller surface error (Fig. 8(*fifth column*)) compared with FLIRT, diffeomorphic Demons, ANTs and DEM (Fig. 8(*first column – fourth column*)). Fig. 9 shows the inter-subject registration results for T1-weighted MR images. The first row shows the 12-month-old template image toward which the moving images at 2 weeks, 3 months and 6 months were deformed. The $2^{nd} - 6^{th}$ rows show the registration results of FLIRT, diffeomorphic Demons, ANTs, DEM and SC-DEM, respectively. Fig. 9 highlights certain regions where SC-DEM yields better alignment than the other methods.

4.1.2. Quantitative evaluation

Registration accuracy was evaluated quantitatively using Dice ratio, computed between the warped moving tissue map (V_1) and the template tissue map (V_2) as

$$\mathrm{D} = \frac{2|V_1 \cap V_2|}{|V_1| + |V_2|} \tag{9}$$

We also computed the modified Hausdorff distance between the cortical surfaces of the warped moving and template images. Let $\mathscr{S}$ and $\mathscr{T}$ be the sets of vertices of the warped moving and template cortical surfaces, respectively. Using the Euclidean distance $d(s,t) = \|s - t\|$, the modified Hausdorff distance (MHD) is given as

$$\mathrm{MHD} = \frac{1}{2}[d(\mathscr{S}, \mathscr{T}) + d(\mathscr{T}, \mathscr{S})], \tag{10}$$

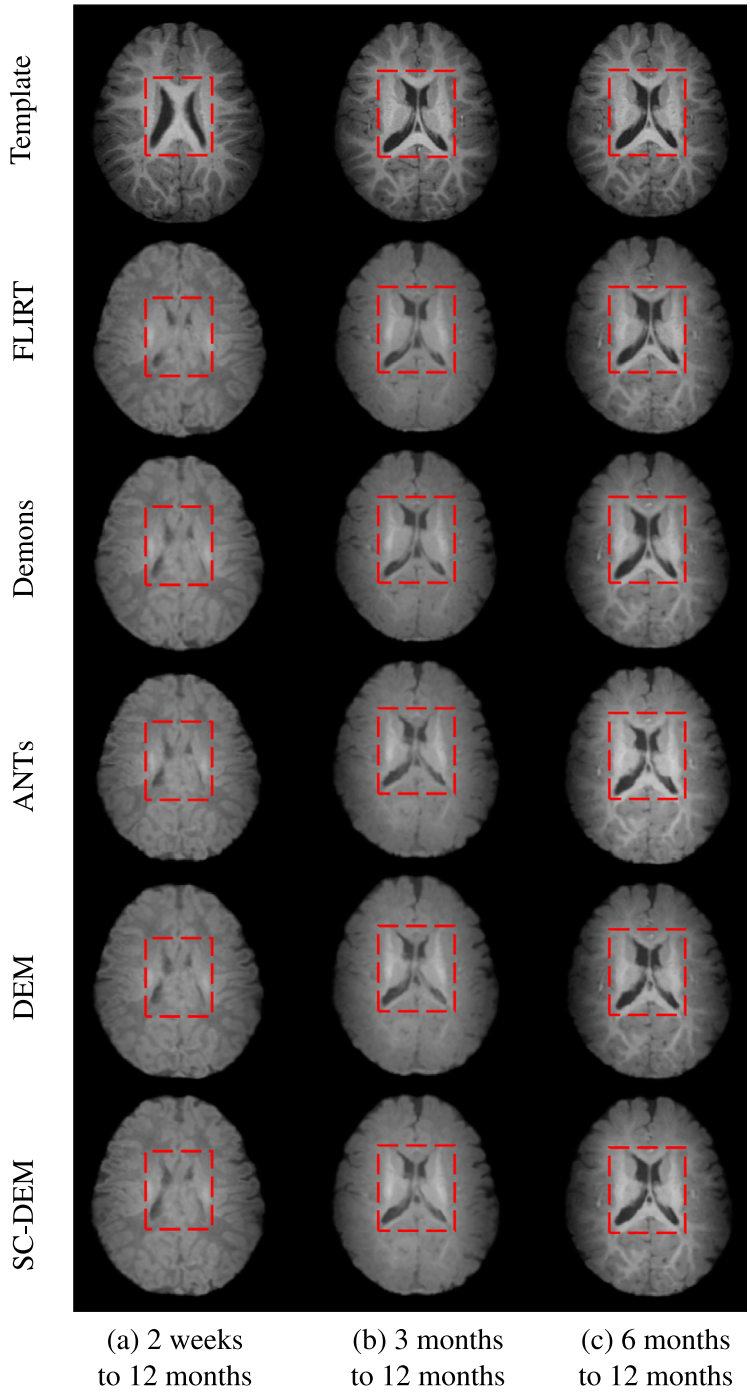

Fig. 15. Moving image warped using FLIRT (*second row*), diffeomorphic Demons (*third row*), ANTs (*fourth row*), DEM (*fifth row*) and SC-DEM (*sixth row*), compared to the template image (*first row*) for intra-subject registration.

where,

$$d(\mathscr{S},\mathscr{T}) = \frac{1}{|\mathscr{S}|}\sum_{s\in\mathscr{S}} d(s,\mathscr{T}) \tag{11}$$

and

$$d(\mathscr{T},\mathscr{S}) = \frac{1}{|\mathscr{T}|}\sum_{t\in\mathscr{T}} d(t,\mathscr{S}) \tag{12}$$

The distances $d(\mathscr{S},\mathscr{T})$ and $d(\mathscr{T},\mathscr{S})$ in Eq. (11) and Eq. (12) are defined as $d(s,\mathscr{T}) = \min_{t\in\mathscr{T}}\|s-t\|$ and $d(t,\mathscr{S}) = \min_{s\in\mathscr{S}}\|t-s\|$.

Fig. 11 shows the Dice ratio box plots for three tissue types at three time points using five different registration methods. It can be observed that SC-DEM achieves the highest Dice ratio with statistical significance ($p < 0.01$) for CSF, GM and WM at all time points. These results are summarized in Table 1. The percent-

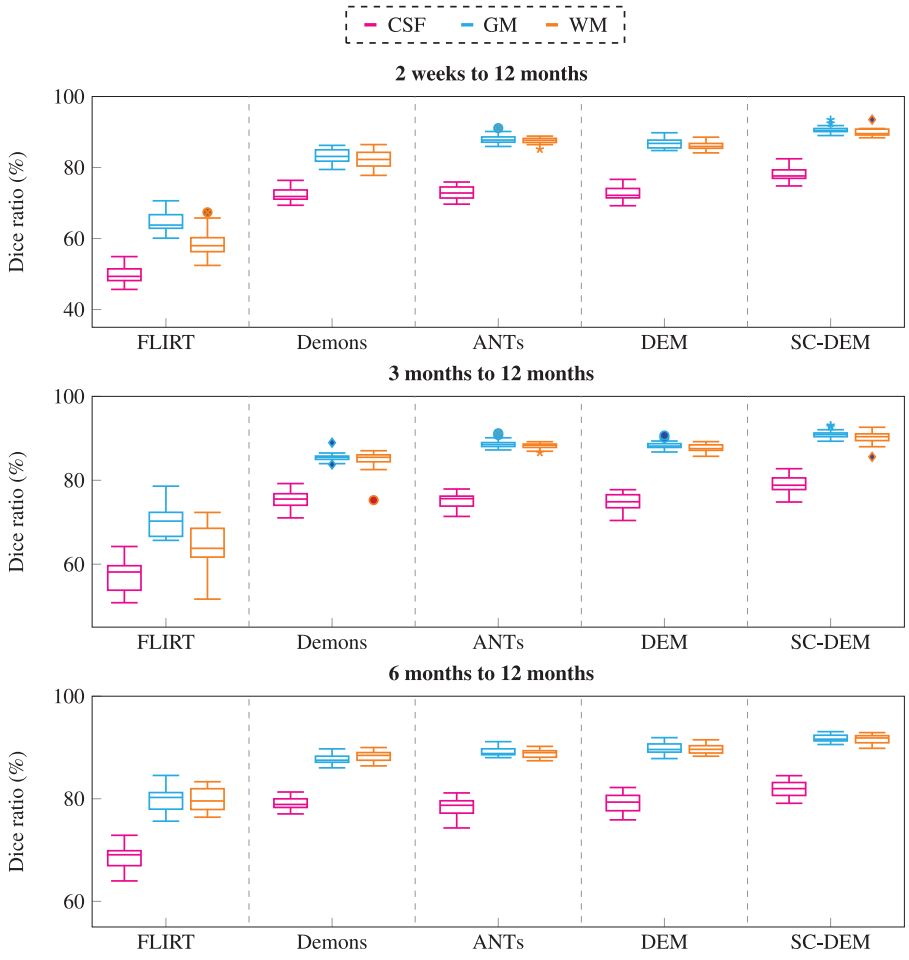

Fig. 16. Intra-subject registration results in terms of Dice ratio for different tissue types (CSF, GM, WM).

ages of improvement over FLIRT for registration from 2 weeks, 3 months, and 6 months to 12 months are 32.76%, 31.85% and 30.33% by diffeomorphic Demons, 41.63%, 40.86% and 39.14% by ANTs, 43.52%, 40.99% and 39.16% by DEM and 53.44%, 53.56% and 50.99% by SC-DEM. In addition, we also computed the Dice ratios for 34 cortical ROIs (see Table 2). These ROIs were automatically labeled by first parcellating the cortical surface using FreeSurfer and then, assgining to each voxel in the GM cortical ribbon a label according to the nearest vertex of the cortical surface. The results, shown in Fig. 10, indicate that SC-DEM yields higher Dice ratios for the majority of the cortical ROIs with statistical significance ($p < 0.01$). We also show the box plots of MHDs computed between the template and warped moving inner and outer cortical surfaces in Fig. 12 for all the registration methods. Table 3 provides the corresponding statistical summary. These results show that SC-DEM achieves the lowest MHD ($p < 0.01$) for all the three time points.

4.2. Intra-subject registration

Intra-subject registration was performed by registering the tissue maps of all the subjects at 2 weeks, 3 months, and 6 months to their respective 12-month tissue maps. All the tissue maps were affinely aligned to the 12-month tissue maps using FLIRT. Diffeomorphic Demons, ANTs and DEM were utilized for comparison.

4.2.1. Qualitative evaluation

Fig. 13 shows that the intra-subject registration results were qualitatively evaluated by visualizing the inner cortical surface of the warped moving image overlaid on the template tissue map. The zoomed-in views show regions where SC-DEM gives clear improvement in structural alignment. Fig. 14(a–c) shows the surface distance (computed using Hausdorff metric) between the warped moving cortical surface at 2 weeks, 3 months, and 6 months and the template cortical surface at 12 months. SC-DEM shows less surface alignment error when compared with other methods. We also present the T1-weighted moving images warped using all the five registration methods in Fig. 15. Due to the low contrast between GM and WM, visualizing improvement in cortical alignment is challenging. However, Fig. 15(a) shows that SC-DEM yields significant improvement in the alignment of the lateral ventricles.

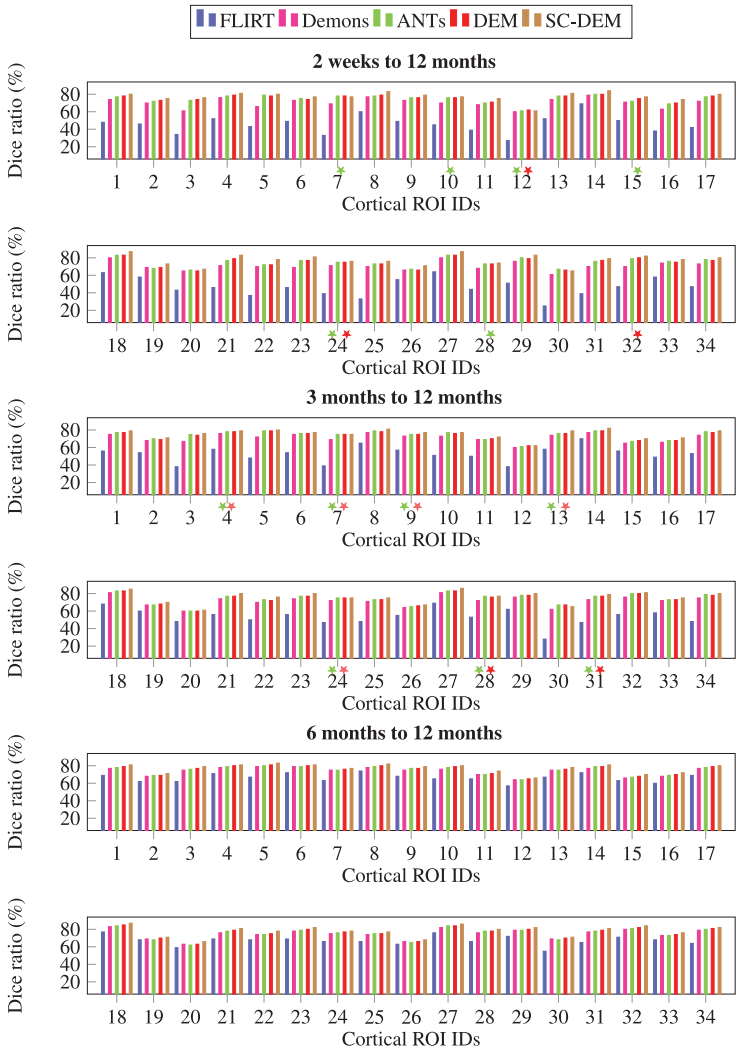

Fig. 17. Intra-subject registration results in terms of Dice ratio for cortical ROIs. The colored stars mark differences that are not statistically significant ($p > .01$) with reference to SC-DEM.

4.2.2. Quantitative evaluation

Intra-subject registration result at 2 weeks, 3 months, and 6 months to 12 months were quantitatively evaluated using Dice ratio and modified Hausdorff distance. The box plots of Dice ratio for CSF, GM and WM achieved by all five registration methods at different time points are presented in Fig. 16. As evident from these box plots, SC-DEM achieves the highest Dice ratio for all tissue types. The statistical summary of whole-brain Dice ratio is presented in Table 4. The overall percentages of improvement over FLIRT registration from 2 weeks, 3 months, and 6 months to 12 months are 37.39%, 27.95% and 11.64% by diffeomorphic Demons, 43.45%, 31.34% and 12.26% by ANTs, 41.72%, 30.56% and 13.36% by DEM and 49.43%, 35.42% and 16.20% by SC-DEM. The Dice ratios for the 34 cortical ROIs, shown in Fig. 17, confirm the superiority of SC-DEM. The MHD box plots for inner and outer cortical surfaces are shown in Fig. 18, with a summary in Table 5. The results again demonstrate the superiority of SC-DEM.

4.3. Computational time

All experiments were conducted on a machine with 3.8 GHz Intel Core i5 and 32 GB RAM. To register a pair of images, SC-DEM took around 1.5 hours, whereas diffeomorphic Demons, ANTs and DEM took around 3-, 20- and 5-minutes, respectively. Although SC-DEM is computationally more expensive, it significantly improves structural alignment.

4.4. Deformation field analysis

We also analyzed the smoothness of the deformation fields. Fig. 19 shows that SC-DEM results in bending energy that is lower than ANTs and DEM. Diffeomorphic Demons gives the lowest bending energy, but performs worst in terms of registration accuracy. The Jacobian maps of the deformation fields for SC-DEM, shown in Fig. 20, indicate that it preserves topology without tearing or shearing artifacts.

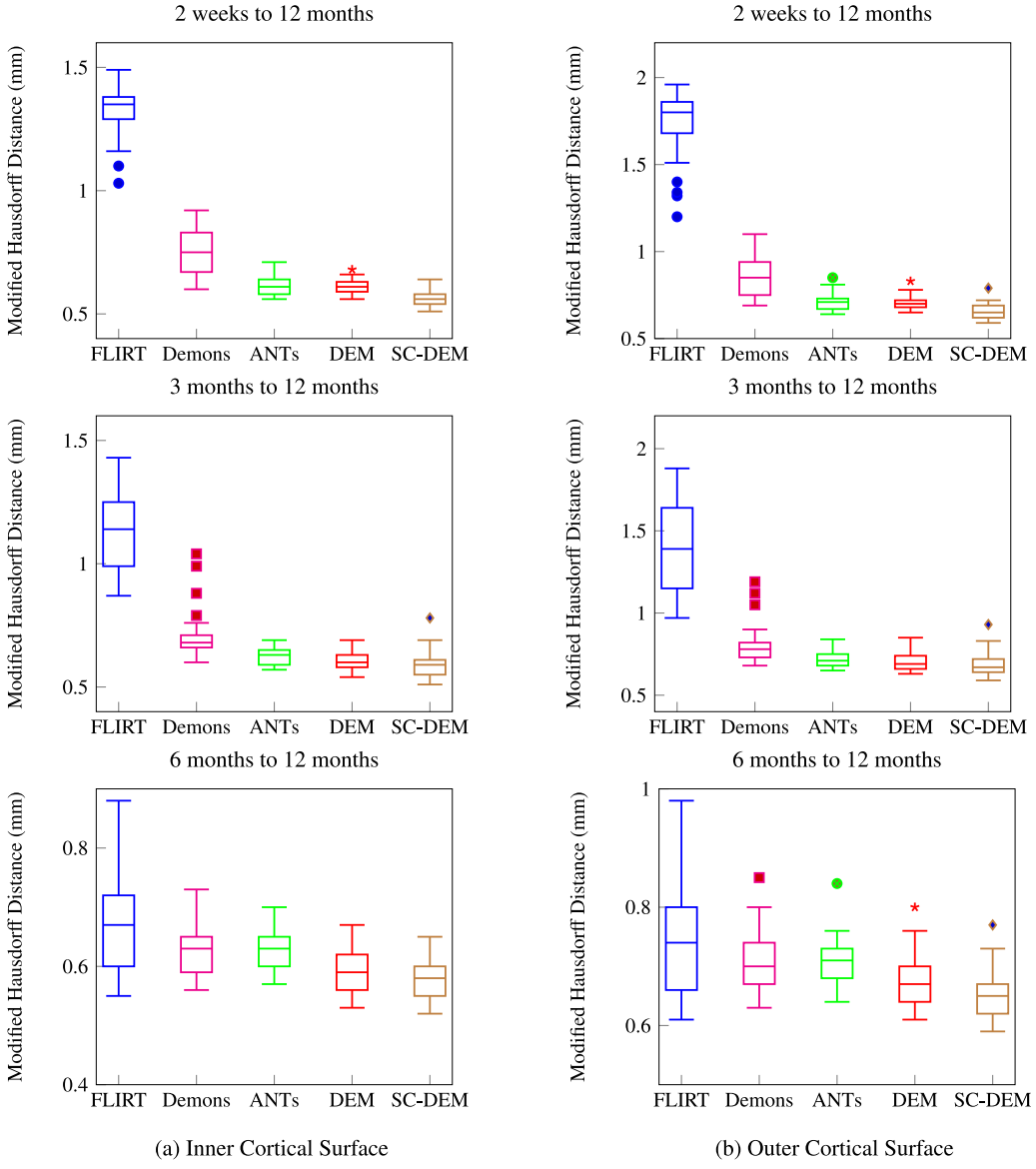

Fig. 18. Intra-subject registration results in terms of modified Hausdorff distance for inner and outer cortical surfaces.

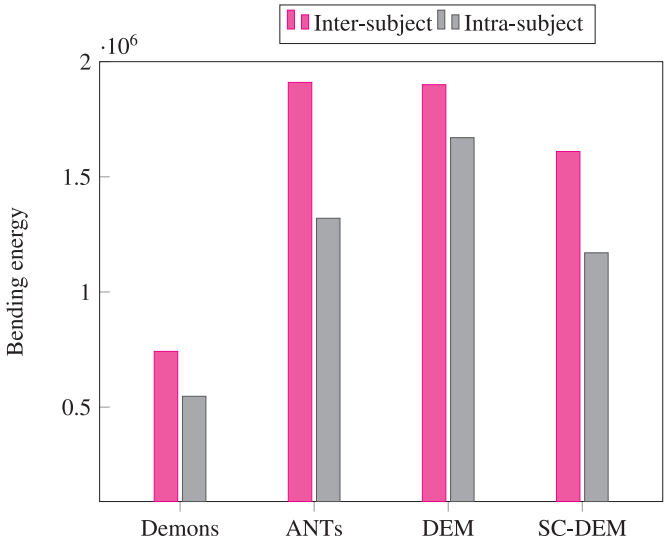

Fig. 19. Bending energy of the deformation fields estimated using different registration methods.

4.5. Parameter sensitivity

In order to evaluate the sensitivity of the proposed method to the parameters, we changed the parameters setting and performed both inter- and intra-subject registration experiments. More specifically, we doubled the value of volumetric force field parameter β to 2.1 and halved the value of surface force field parameter γ to 1×10^{-4} in order to balance the two force fields. γ was incremented with $\Delta\gamma = 1 \times 10^{-4}$ and the regularization parameter α was decreased with a step size of $\Delta\alpha = 0.004$. The rest of the parameters were kept the same as described in Section 3.3. The results in terms of Dice ratio and modified Hausdorff distance are presented in Fig. 21, where P_1 denotes old parameters setting and P_2 denotes new setting. The paired t-test indicates that there is no statistically significant difference ($p > 0.01$) between the Dice ratios (as well as MHDs) of two parameters settings. This validates that our method is insensitive to the change in parameters. We show in Table 6 the range of parameters that can be used to obtain comparable registration performance.

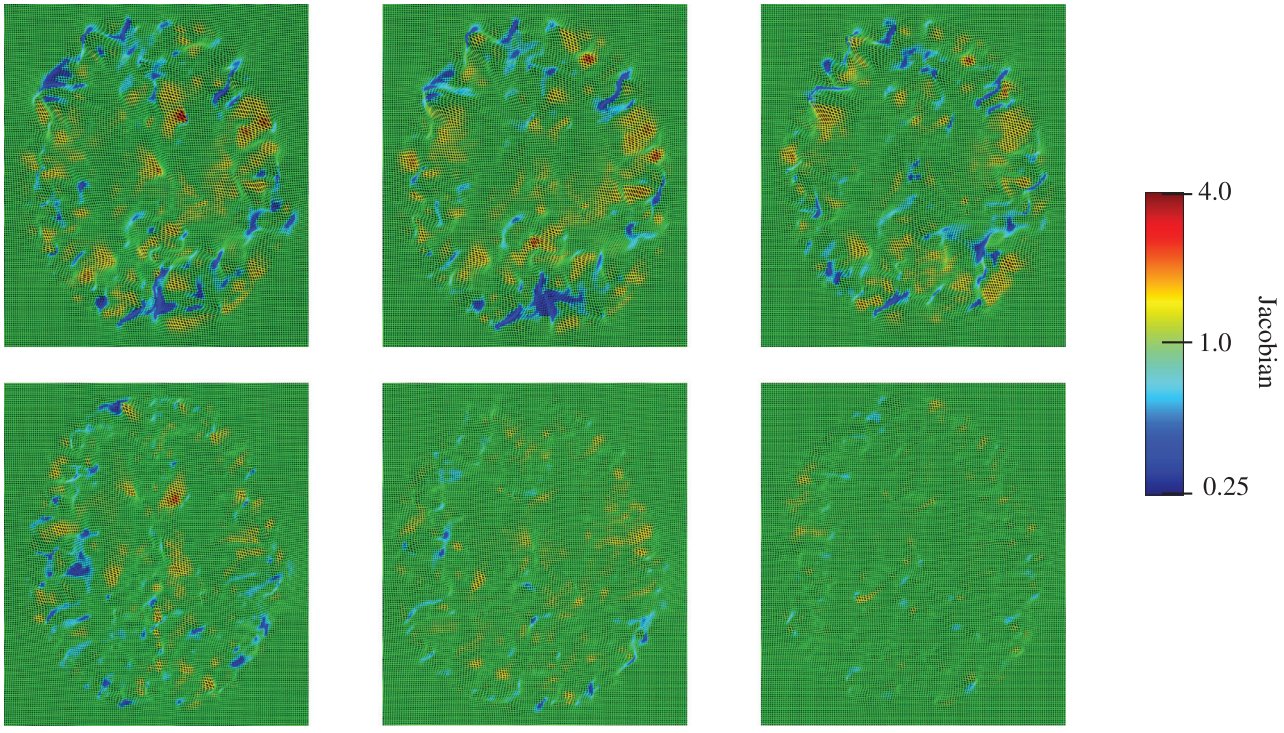

Fig. 20. Deformation Jacobian maps of SC-DEM for inter-subject (*first row*) and intra-subject (*second row*) registration.

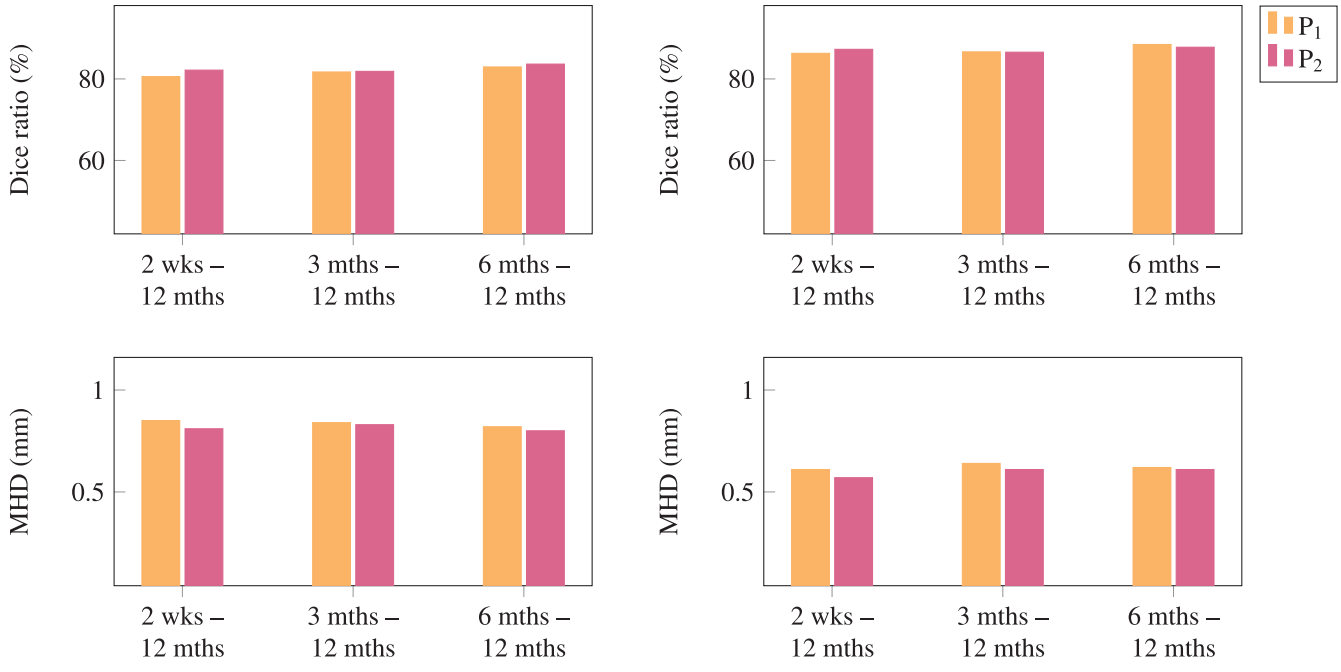

Fig. 21. Parameter sensitivity analysis in terms of Dice ratio and modified Hausdorff distance.

5. Conclusion

In this paper, we presented an infant brain MRI registration framework for consistently aligning the cortical folding patterns and subcortical structures. First, the cortical surfaces are registered to obtain accurate surface correspondence. Then, the estimated surface correspondence is used to constrain the volumetric registration based on a dynamic elasticity model, resulting in the alignment of both brain volume and cortical folds. Despite limited in the number of subjects, evaluation was conducted rigorously for inter- and intra-subject registration from 2 weeks, 3 months, and 6 months to 12 months, involving over a hundred registration experiments. The results demonstrate that the proposed method yields superior performance in both volumetric and surface registration.

Declaration of Competing Interest

None declared.

Acknowledgments

This work was supported in part by NIH grants (AG053867, EB008374, MH117943).

References

Acosta, O., Fripp, J., Rueda, A., Xiao, D., Bonner, E., Bourgeat, P., Salvado, O., 2010. 3D shape context surface registration for cortical mapping. In: IEEE International Symposium on Biomedical Imaging: From Nano to Macro (ISBI'10). Rotterdam, Netherlands, pp. 1021–1024. doi:10.1109/ISBI.2010.5490163.

Ahmad, S., Khan, M.F., 2017. Dynamic elasticity model for inter-subject non-rigid registration of 3D MRI brain scans. Biomed. Signal Process. Control 33, 346–357. doi:10.1016/j.bspc.2016.12.016.

Ahmad, S., Wu, Z., Li, G., Wang, L., Lin, W., Yap, P.-T., Shen, D., 2019. Surface-volume consistent construction of longitudinal atlases for the early developing brains. In: Shen, D., Liu, T. (Eds.), Medical Image Computing and Computer Assisted Intervention - MICCAI 2019. Springer.

Avants, B., Epstein, C., Grossman, M., Gee, J., 2008. Symmetric diffeomorphic image registration with cross-correlation: evaluating automated labeling of elderly and neurodegenerative brain. Med. Image Anal. 12 (1), 26–41. doi:10.1016/j.media.2007.06.004.

Budday, S., Nay, R., de Rooij, R., Steinmann, P., Wyrobek, T., Ovaert, T.C., Kuhl, E., 2015. Mechanical properties of gray and white matter brain tissue by indentation. J. Mech. Behav. Biomed.Mater. 46, 318–330. doi:10.1016/j.jmbbm.2015.02.024.

Chen, M., Carass, A., Jog, A., Lee, J., Roy, S., Prince, J.L., 2017. Cross contrast multi-channel image registration using image synthesis for MR brain images. Med. Image Anal. 36, 2–14. doi:10.1016/j.media.2016.10.005.

Choe, M.-s., Ortiz-Mantilla, S., Makris, N., Gregas, M., Bacic, J., Haehn, D., Kennedy, D., Pienaar, R., Caviness Jr, V.S., Benasich, A.A., Grant, P.E., 2013. Regional infant brain development: an MRI-based morphometric analysis in 3 to 13 month olds. Cereb. Cortex 23 (9), 2100–2117. doi:10.1093/cercor/bhs197.

Dale, A.M., Fischl, B., Sereno, M.I., 1999. Cortical surface-based analysis: I. segmentation and surface reconstruction. NeuroImage 9 (2), 179–194. doi:10.1006/nimg.1998.0395.

Fischl, B., Sereno, M.I., Dale, A.M., 1999. Cortical surface-based analysis: II: inflation, flattening, and a surface-based coordinate system. NeuroImage 9 (2), 195–207. doi:10.1006/nimg.1998.0396.

Geng, X., Li, G., Lu, Z., Gao, W., Wang, L., Shen, D., Zhu, H., Gilmore, J.H., 2017. Structural and maturational covariance in early childhood brain development. Cereb. Cortex 27 (3), 1795–1807. doi:10.1093/cercor/bhw022.

Gholipour, A., Kehtarnavaz, N., Briggs, R., Devous, M., Gopinath, K., 2007. Brain functional localization: a survey of image registration techniques. IEEE Trans. Med. Imag. 26 (4), 427–451. doi:10.1109/TMI.2007.892508.

Gilmore, J.H., Knickmeyer, R.C., Gao, W., 2018. Imaging structural and functional brain development in early childhood. Nature Rev. Neurosci. 19, 123–137. doi:10.1038/nrn.2018.1.

Hazlett, H.C., Gu, H., Munsell, B.C., Kim, S.H., Styner, M., Wolff, J.J., Elison, J.T., Swanson, M.R., Zhu, H., Botteron, K.N., Collins, D.L., Constantino, J.N., Dager, S.R., Estes, A.M., Evans, A.C., Fonov, V.S., Gerig, G., Kostopoulos, P., McKinstry, R.C., Pandey, J., Paterson, S., Pruett, J.R., Schultz, R.T., Shaw, D.W., Zwaigenbaum, L., Piven, J., for the IBIS Network, 2017. Early brain development in infants at high risk for autism spectrum disorder. Nature 542 (7641), 348–351. doi:10.1038/nature21369.

Hellier, P., Barillot, C., Corouge, I., Gibaud, B., Goualher, G.L., Collins, D.L., Evans, A., Malandain, G., Ayache, N., Christensen, G.E., Johnson, H.J., 2003. Retrospective evaluation of intersubject brain registration. IEEE Trans. Med. Imag. 22 (9), 1120–1130. doi:10.1109/TMI.2003.816961.

Jenkinson, M., Bannister, P., Brady, M., Smith, S., 2002. Improved optimization for the robust and accurate linear registration and motion correction of brain images. NeuroImage 17 (2), 825–841. doi:10.1006/nimg.2002.1132.

Jenkinson, M., Smith, S., 2001. A global optimisation method for robust affine registration of brain images. Med. Image Anal. 5 (2), 143–156. doi:10.1016/S1361-8415(01)00036-6.

Joshi, A.A., Shattuck, D.W., Leahy, R.M., 2012. A method for automated cortical surface registration and labeling. In: Dawant, B.M., Christensen, G.E., Fitzpatrick, J.M., Rueckert, D. (Eds.), Biomedical Image Registration. Springer Berlin Heidelberg, Berlin, Heidelberg, pp. 180–189. doi:10.1007/978-3-642-31340-0_19.

Joshi, A.A., Shattuck, D.W., Thompson, P.M., Leahy, R.M., 2007. Surface-constrained volumetric brain registration using harmonic mappings. IEEE Trans. Med. Imag. 26 (12), 1657–1669. doi:10.1109/TMI.2007.901432.

Kim, M., Wu, G., Wang, Q., Lee, S.-W., Shen, D., 2015. Improved image registration by sparse patch-based deformation estimation. NeuroImage 105, 257–268. doi:10.1016/j.neuroimage.2014.10.019.

Knickmeyer, R.C., Gouttard, S., Kang, C., Evans, D., Wilber, K., Smith, J.K., Hamer, R.M., Lin, W., Gerig, G., Gilmore, J.H., 2008. A structural MRI study of human brain development from birth to 2 years. J. Neurosci. Offic. J. Soc. Neurosci. 28, 12176–12182. doi:10.1523/JNEUROSCI.3479-08.2008.

Li, G., Lin, W., Gilmore, J.H., Shen, D., 2015a. Spatial patterns, longitudinal development, and hemispheric asymmetries of cortical thickness in infants from birth to 2 years of age. J. Neurosci. 35 (24), 9150–9162. doi:10.1523/JNEUROSCI.4107-14.2015.

Li, G., Nie, J., Wang, L., Shi, F., Gilmore, J.H., Lin, W., Shen, D., 2014a. Measuring the dynamic longitudinal cortex development in infants by reconstruction of temporally consistent cortical surfaces. NeuroImage 90, 266–279. doi:10.1016/j.neuroimage.2013.12.038.

Li, G., Nie, J., Wang, L., Shi, F., Gilmore, J.H., Lin, W., Shen, D., 2013. Mapping region-specific longitudinal cortical surface expansion from birth to 2 years of age. Cereb. Cortex 23 (11), 2724–2733. doi:10.1093/cercor/bhs265.

Li, G., Nie, J., Wang, L., Shi, F., Lyall, A.E., Lin, W., Gilmore, J.H., Shen, D., 2014b. Mapping longitudinal hemispheric structural asymmetries of the human cerebral cortex from birth to 2 years of age. Cereb. Cortex 24 (5), 1289–1300. doi:10.1093/cercor/bhs413.

Li, G., Nie, J., Wu, G., Wang, Y., Shen, D., 2012. Consistent reconstruction of cortical surfaces from longitudinal brain MR images. NeuroImage 59 (4), 3805–3820. doi:10.1016/j.neuroimage.2011.11.012.

Li, G., Wang, L., Shi, F., Gilmore, J.H., Lin, W., Shen, D., 2015b. Construction of 4D high-definition cortical surface atlases of infants: methods and applications. Med. Image Anal. 25 (1), 22–36. doi:10.1016/j.media.2015.04.005.

Li, G., Wang, L., Shi, F., Lyall, A.E., Lin, W., Gilmore, J.H., Shen, D., 2014c. Mapping longitudinal development of local cortical gyrification in infants from birth to 2 years of age. J. Neurosci. 34 (12), 4228–4238. doi:10.1523/JNEUROSCI.3976-13.2014.

Li, G., Wang, L., Yap, P.-T., Wang, F., Wu, Z., Meng, Y., Dong, P., Kim, J., Shi, F., Rekik, I., Lin, W., Shen, D., 2018. Computational neuroanatomy of baby brains: a review. NeuroImage doi:10.1016/j.neuroimage.2018.03.042.

Lyall, A.E., Shi, F., Geng, X., Woolson, S., Li, G., Wang, L., Hamer, R.M., Shen, D., Gilmore, J.H., 2015. Dynamic development of regional cortical thickness and surface area in early childhood. Cereb. Cortex 25 (8), 2204–2212. doi:10.1093/cercor/bhu027.

Matsuzawa, J., Matsui, M., Konishi, T., Noguchi, K., Gur, R.C., Bilker, W., Miyawaki, T., 2001. Age-related volumetric changes of brain gray and white matter in healthy infants and children. Cereb. Cortex 11 (4), 335–342. doi:10.1093/cercor/11.4.335.

Meng, Y., Li, G., Lin, W., Gilmore, J.H., Shen, D., 2014. Spatial distribution and longitudinal development of deep cortical sulcal landmarks in infants. NeuroImage 100, 206–218. doi:10.1016/j.neuroimage.2014.06.004.

Nie, J., Li, G., Shen, D., 2013. Development of cortical anatomical properties from early childhood to early adulthood. NeuroImage 76, 216–224. doi:10.1016/j.neuroimage.2013.03.021.

Nie, J., Li, G., Wang, L., Gilmore, J.H., Lin, W., Shen, D., 2012. A computational growth model for measuring dynamic cortical development in the first year of life. Cereb. Cortex 22 (10), 2272–2284. doi:10.1093/cercor/bhr293.

Nie, J., Li, G., Wang, L., Shi, F., Lin, W., Gilmore, J.H., Shen, D., 2014. Longitudinal development of cortical thickness, folding, and fiber density networks in the first 2 years of life. Hum. Brain Map. 35 (8), 3726–3737. doi:10.1002/hbm.22432.

Park, H., Park, J.-S., Seong, J.-K., Na, D.L., Lee, J.-M., 2012. Cortical surface registration using spherical thin-plate spline with sulcal lines and mean curvature as features. J. Neurosci. Methods 206 (1), 46–53. doi:10.1016/j.jneumeth.2012.02.010.

Paterson, S.J., Heim, S., Friedman, J.T., Choudhury, N., Benasich, A.A., 2006. Development of structure and function in the infant brain: implications for cognition, language and social behaviour. Neurosci. Biobehav. Rev. 30 (8), 1087–1105. doi:10.1016/j.neubiorev.2006.05.001.

Postelnicu, G., Zöllei, L., Fischl, B., 2009. Combined volumetric and surface registration. IEEE Trans. Med. Imag. 28 (4), 508–522. doi:10.1109/TMI.2008.2004426.

Shen, D., Davatzikos, C., 2002. HAMMER: hierarchical attribute matching mechanism for elastic registration. IEEE Trans. Med. Imag. 21 (11), 1421–1439. doi:10.1109/TMI.2002.803111.

Shi, F., Wang, L., Dai, Y., Gilmore, J.H., Lin, W., Shen, D., 2012. LABEL: pediatric brain extraction using learning-based meta-algorithm. NeuroImage 62 (3), 1975–1986. doi:10.1016/j.neuroimage.2012.05.042.

Shi, J., Wang, Y., Ceschin, R., An, X., Lao, Y., Vanderbilt, D., Nelson, M.D., Thompson, P.M., Panigrahy, A., Leporé, N., 2013. A multivariate surface-based analysis of the putamen in premature newborns: regional differences within the ventral striatum. PLOS ONE 8 (7), 1–9. doi:10.1371/journal.pone.0066736.

Sled, J.G., Zijdenbos, A.P., Evans, A.C., 1998. A nonparametric method for automatic correction of intensity nonuniformity in MRI data. IEEE Trans. Med. Imag. 17 (1), 87–97. doi:10.1109/42.668698.

Tang, S., Cong, W., Yang, J., Fu, T., Song, H., Ai, D., Wang, Y., 2018. Local statistical deformation models for deformable image registration. Neurocomputing (In Press) doi:10.1016/j.neucom.2018.03.039.

Vercauteren, T., Pennec, X., Perchant, A., Ayache, N., 2009. Diffeomorphic demons: efficient non-parametric image registration. NeuroImage 45 (1, Supplement 1), S61–S72. doi:10.1016/j.neuroimage.2008.10.040.

Wang, L., Gao, Y., Shi, F., Li, G., Gilmore, J.H., Lin, W., Shen, D., 2015a. LINKS: Learning-based multi-source IntegratioN frameworK for Segmentation of infant brain images. NeuroImage 108, 160–172. doi:10.1016/j.neuroimage.2014.12.042.

Wang, Q., Kim, M., Shi, Y., Wu, G., Shen, D., 2015b. Predict brain MR image registration via sparse learning of appearance and transformation. Med. Image Anal. 20 (1), 61–75. doi:10.1016/j.media.2014.10.007.

Wei, L., Cao, X., Wang, Z., Gao, Y., Hu, S., Wang, L., Wu, G., Shen, D., 2017. Learning-based deformable registration for infant MRI by integrating random forest with auto-context model. Med. Phys. 44 (12), 6289–6303. doi:10.1002/mp.12578.

Wu, G., Kim, M., Wang, Q., Munsell, B.C., Shen, D., 2016. Scalable high-performance image registration framework by unsupervised deep feature representations learning. IEEE Trans. Biomed. Eng. 63 (7), 1505–1516. doi:10.1109/TBME.2015.2496253.

Wu, G., Qi, F.Q., Shen, D., 2006. Learning-based deformable registration of MR brain images. IEEE Trans. Med. Imag. 25 (9), 1145–1157. doi:10.1109/TMI.2006.879320.

Wu, Y., Wu, G., Wang, L., Munsell Brent, C., Wang, Q., Lin, W., Feng, Q., Chen, W., Shen, D., 2015. Hierarchical and symmetric infant image registration by robust longitudinal-example-guided correspondence detection. Med. Phys. 42 (7), 4174–4189. doi:10.1118/1.4922393.

Xue, H., Srinivasan, L., Jiang, S., Rutherford, M., Edwards, A.D., Rueckert, D., Hajnal, J.V., 2007. Automatic segmentation and reconstruction of the cortex from neonatal MRI. NeuroImage 38 (3), 461–477. doi:10.1016/j.neuroimage.2007.07.030.

Xue, Z., Shen, D., Davatzikos, C., 2006a. Statistical representation of high-dimensional deformation fields with application to statistically constrained 3D warping. Med. Image Anal. 10 (5), 740–751. doi:10.1016/j.media.2006.06.007.

Xue, Z., Shen, D., Karacali, B., Stern, J., Rottenberg, D., Davatzikos, C., 2006b. Simulating deformations of MR brain images for validation of atlas-based segmentation and registration algorithms. NeuroImage 33 (3), 855–866. doi:10.1016/j.neuroimage.2006.08.007.

Yang, X., Kwitt, R., Styner, M., Niethammer, M., 2017. Quicksilver: fast predictive image registration - a deep learning approach. NeuroImage 158, 378–396. doi:10.1016/j.neuroimage.2017.07.008.

Yeo, B.T.T., Sabuncu, M.R., Vercauteren, T., Ayache, N., Fischl, B., Golland, P., 2010. Spherical demons: fast diffeomorphic landmark-free surface registration. IEEE Trans. Med. Imag. 29 (3), 650–668. doi:10.1109/TMI.2009.2030797.

Zöllei, L., Stevens, A., Huber, K., Kakunoori, S., Fischl, B., 2010. Improved tractography alignment using combined volumetric and surface registration. NeuroImage 51 (1), 206–213. doi:10.1016/j.neuroimage.2010.01.101.

Zou, G., Hua, J., Muzik, O., 2007. Non-rigid surface registration using spherical thin-plate splines. In: Ayache, N., Ourselin, S., Maeder, A. (Eds.), Medical Image Computing and Computer-Assisted Intervention - MICCAI 2007. Springer Berlin Heidelberg, Berlin, Heidelberg, pp. 367–374. doi:10.1007/978-3-540-75757-3_45.